Journal of Materials Chemistry A

Materials for energy and sustainability

Accepted Manuscript

This article can be cited before page numbers have been issued, to do this please use: A. Kutty and Y. Song, *J. Mater. Chem. A*, 2025, DOI: 10.1039/D5TA07554H.



This is an Accepted Manuscript, which has been through the Royal Society of Chemistry peer review process and has been accepted for publication.

Accepted Manuscripts are published online shortly after acceptance, before technical editing, formatting and proof reading. Using this free service, authors can make their results available to the community, in citable form, before we publish the edited article. We will replace this Accepted Manuscript with the edited and formatted Advance Article as soon as it is available.

You can find more information about Accepted Manuscripts in the <u>Information for Authors</u>.

Please note that technical editing may introduce minor changes to the text and/or graphics, which may alter content. The journal's standard <u>Terms & Conditions</u> and the <u>Ethical guidelines</u> still apply. In no event shall the Royal Society of Chemistry be held responsible for any errors or omissions in this Accepted Manuscript or any consequences arising from the use of any information it contains.



Pressure-Tuned 2D Hybrid Perovskites: Emerging Insights and Future Opportunities

Aditya Kutty¹ and Yang Song^{1,2,*}

- ¹ Department of Chemistry, University of Western Ontario, London, Ontario, N6A 5B7
- ² Department of Physics and Astronomy, University of Western Ontario, London, Ontario, N6A 3K7

Abstract

Two-dimensional (2D) hybrid organic–inorganic perovskites (HOIPs) are attracting growing attention for their exceptional structural flexibility, environmental stability, and unique quantum confinement effects. While chemical design has dominated the field, high-pressure techniques are emerging as a powerful, non-invasive route to tune lattice structures and optoelectronic responses in situ. Here, we present our perspective on the rapidly developing landscape of pressure-tuned 2D perovskites, focusing on Ruddlesden–Popper (RP) and Dion–Jacobson (DJ) systems. We highlight recent discoveries of pressure-induced structural phase transitions, direct–indirect bandgap conversions, broadband emission from self-trapped excitons, and the stabilization of metastable states. Particular emphasis is placed on contrasting soft vs. rigid organic spacers and lead-based vs. lead-free systems (Sn, Cu, Ge, Bi). We argue that pressure not only serves as a diagnostic tool but also as a synthetic strategy for accessing hidden phases and functionalities. Looking ahead, the convergence of high-pressure spectroscopy, synchrotron techniques, and computational modeling offers exciting opportunities to rationally engineer sustainable, pressure-responsive optoelectronic materials.

Keywords

Two-dimensional perovskites; high pressure; diamond anvil cell; Ruddlesden-Popper; Dion-Jacobson; phase transition; photoluminescence; bandgap tuning; optoelectronic properties

^{*}yang.song@uwo.ca

1. Why Pressure Matters for 2D Perovskites

Over the years, the application of halide perovskites in the field of optoelectronics has increased substantially owing to significant improvement of their photovoltaic performance.¹ As such, perovskites have garnered high interest in a number of optoelectronic applications, with the most prominent to date being solar cells.^{2–4} Halide perovskites typically exist in either the three-dimensional (3D) or two-dimensional (2D) form, with 3D halide perovskites adopting an ABX₃ structure (where A is a small monovalent cation such as MA⁺ or Cs⁺, B is Pb²⁺ or Sn²⁺, and X is a halide).^{5,6} 3D perovskites have been shown to exhibit excellent light absorption,^{7,8} long charge-carrier diffusion lengths,^{9,10} and high defect tolerance.¹¹ However, 3D perovskites suffer from limited stability, restricted chemical composition, sensitivity to moisture and light, and the use of highly volatile and toxic cations.^{12,13} To address these limitations, low-dimensional (especially 2D) perovskites have been explored.^{6,13–15}

In comparison to 3D perovskites, 2D perovskites exhibit greater stability towards humidity and light, and they tend to use bigger, less volatile organic cations (typically hydrophobic) which enhances both the thermal and chemical stability.¹³ In general, 2D hybrid organic-inorganic perovskites (HOIPs) adopt the following formula $(A')_m A_{n-1} B_n X_{3n+1}$ (Figure 1a), where A' is the organic spacer cation and can be either monovalent (m = 2) or divalent (m = 1), and n (or thickness) is the number of metal-halide octahedra between the adjacent organic layers. 6,13,16 The specific arrangement of the organic-inorganic layers forms a 2D multiple quantum well (MQW) electronic structure (Figure 1b) with the organic spacers acting as insulating barriers, thus restricting the charge carriers in two dimensions.⁶ This structure introduces both quantum and dielectric confinement effects, due to the difference in permittivity between ionic perovskite layer and bulky organic cation, ¹⁷ while the organic layers provide environmental shielding, enhancing moisture resistance, and thermal stability. Depending on the structure of the organic spacer, 2D perovskites can adopt Ruddlesden-Popper (RP, typically monovalent spacers) (Figure 1c), Dion-Jacobson (DJ, typically divalent spacers) (Figure 1c), or alternating-cation layered perovskite phases (ACI) (Figure 1c). 6,13,18 RP phases contain metal-halide inorganic layers separated by bilayers of bulky ammonium spacer cations via weak van der Waals interactions, ¹³ allowing for greater interlayer distances and isolated layers exhibiting no perovskite-perovskite interactions, ⁶ while adopting a $(A')_2(A)_{n-1}B_nX_{3n+1}$ formula. 16 In contrast, DJ phases contain inorganic layers which stack directly on top of each other and employ bifunctional spacer cations, allowing direct bonding between layers, 13 and the close proximity of the layers enables weak perovskite-perovskite interactions, 6 while adopting a $(A')(A)_{n-1}B_nX_{3n+1}$ formula. 18 The ACI phase, a subclass of the DJ phase, employ alternating organic cation, typically guanidinium (GA) and methylammonium (MA), in the interlayer space, thus stabilizing the structure and adopting a $(A')_2(A)_nB_nX_{3n+1}$ formula. 13 In recent years, significant efforts have gone into understanding and tuning the optoelectronic behavior of 2D perovskites, in particular through physical approaches. Most notably, high pressure has emerged as a powerful tool to continuously modulate both the structures and optoelectronic properties of 2D metal-halide perovskites without altering their composition. $^{19-}$

Figure 1. Structure of 2D HOIPs. (a) Crystal structure for n = 1, 2, and 3 and (b) electronic structure showing 2D multiple quantum well. Reproduced from ref. 6 with permission from American Chemical Society, copyright 2018. (c) RP, DJ, Reproduced from ref. 13 with permission from Wiley-VCH GmbH, copyright 2019. and alternating cation 2D HOIP crystal structure. Reproduced from ref. 6 with permission from American Chemical Society, copyright 2018. (d) effect of external pressure on Pb-I-Pb bond angle and Pb-I bond length. Reproduced from ref. 47 with permission from PNAS, copyright 2018.

High pressure can modulate changes to the structures of 2D perovskites resulting in distortion of the crystal lattice, depending on the direction of the applied external pressure, and subsequent octahedral tilting, bond contraction, and bond angle shortening,⁶ whilst the earliest known account of pressure-induced octahedral tilting and bond contraction of 2D perovskites was on (EA)₂CuCl₄ in 1994.⁴⁸ In halide perovskites, compression results in relaxation of the inorganic lattice occurs through bond contraction and octahedral tilting, with the former typically dominating at low pressures (≤ ~ 2−3 GPa), while the latter tends to dominate at moderate to high pressure (~ 3−8 GPa).⁴⁹ Such structural changes are often governed by changes in the Pb-X-Pb bond angles and Pb-X bond lengths, such as in lead-iodide 2D perovskites where these changes result from narrowing of the Pb-I-Pb bond angle and shortening of the Pb-I bond length.⁴⁷ Structural changes subsequently result in changes to the optoelectronic properties with narrowing of the Pb-I-Pb bond angle leading to bandgap widening, whilst shortening of the Pb-I bond length leading to bandgap narrowing, as seen in Figure 1d.⁴⁷ Such changes can reduce interlayer spacing, and in some cases trigger irreversible structural rearrangements or amorphization. The onset of these transitions is

Open Access Article. Published on 28 Mphalane 2025. Downloaded on 2025-11-04 19:45:23.

PY-NO. This article is licensed under a Creative Commons Attribution-NonCommercial 3.0 Unported Licence

typically lower in 2D HOIPs compared to their 3D counterparts, due to greater structural softness. For more complicated 2D HOIP structures especially those with n>1, the intralayer and interlayer organic structures and their interplay with Pb-I octahedra needs to be considered to understand the structure-optoelectronic property relationship.³⁹ High-pressure studies are particularly attractive because they not only allow for the modification of both the structures and optoelectronic properties but can also reveal rare pressure-induced phenomena. 47,50-56 In particular, high pressure has been shown to induce direct-to-indirect bandgap shifts,⁵¹ broadband emission from selftrapped excitons, 52,55,56 hidden polymorphs, 47,55,56 the presence of metastable phases with enhanced properties, 47,50,53 and pressure-induced metallization in perovskite compositions.⁵⁴ In recent years several reviews have begun to map out the broader landscape of pressure tuning in perovskite materials. 57-59 However, no dedicated review has yet focused exclusively on 2D perovskites, in particular comparing RP and DJ types or systematically exploring the behavior of lead-based and lead-free systems under pressure. Our work aims to fill that gap by offering a detailed synthesis of high-pressure behavior in 2D perovskites, focusing on structural transitions, bandgap evolution, and the relationship between mechanical stress and optoelectronic properties. A roadmap schematic of pressure effects on 2D HOIPs is shown in Figure 2.

Figure 2. Schematic roadmap of pressure effects in 2D hybrid perovskites. At the center, the diamond anvil cell (DAC) symbolizes pressure as an external tuning knob. Sequential arrows highlight the cascade of responses under compression: (i) structural changes such as phase transitions, octahedral tilting, and eventual amorphization; Reproduced from ref. 36 with permission from American Chemical Society, copyright 2023. (ii) electronic effects including bandgap narrowing, anomalous widening, and direct—indirect conversions; Reproduced from ref. 53 with permission from Wiley-VCH GmbH, copyright 2020. (iii) optical responses ranging from photoluminescence enhancement to broadband self-trapped exciton (STE) emission; Reproduced from ref. 45 with permission from Wiley-VCH GmbH, copyright 2025. (iv) metastable states where narrowed gaps or persistent PL remain after decompression. Reproduced from ref. 53 with permission from Wiley-VCH GmbH, copyright 2020. Together, these links illustrate how pressure serves not only as a probe but also as a design pathway for uncovering and stabilizing functional states in 2D perovskites.

We begin by classifying the structural motifs of 2D perovskites, and then introduce the experimental tools and techniques used in high-pressure research (Section 2). Subsequent sections detail pressure-induced structural phase transitions of both RP and DJ systems (Section 3), and evolution of optical and electronic properties of RP and DJ systems (Section 4). We also highlight

the growing interest in lead-free 2D perovskites (Section 5) and conclude with a forward-looking outlook (Section 6).

2. How We Study 2D Perovskites Under Pressure

Diamond, being the hardest natural material on earth, is capable of withstanding very high pressures and exhibits excellent transparency to both visible light and x-rays, thus making the diamond anvil cell (DAC) the optimal tool for performing in situ high pressure measurements. 60,61 For 2D perovskites, single-crystal and polycrystalline samples are compressed between the culets of opposing diamonds, often with a ruby chip (Cr³⁺ doped Al₂O₃, Al₂O₃: Cr³⁺) for pressure calibration (via fluorescence shift) and a pressure-transmitting medium (e.g., silicone oil, inert gases such as He, Ne, or Ar, and N₂) to maintain hydrostatic or quasi-hydrostatic conditions.^{60,62} A schematic of a typical DAC can be seen in Figure 3a. In terms of the experimental methods, pressure-induced phase transitions and unit cell evolution are often revealed using synchrotron Xray diffraction (XRD) with Raman and infrared spectroscopy (FTIR) able to provide further confirmation of the phase transitions along with pressure-induced changes in organic cation vibrations, octahedral tilting, and lattice strain. 36,45 The typical Raman and IR setup can be seen in Figure 3b and 3c. In situ optical absorption (UV-Vis) and photoluminescence (PL) spectroscopy track bandgap modulation and excitonic responses upon compression, 36,45 while time resolved photoluminescence (TRPL) can be used to examine charge carrier lifetimes.^{21,34} A general setup for PL and UV-Vis can be seen in Figure 3d. In addition to experimental studies, computational studies, typically through density functional theory (DFT) calculations, can provide further confirmation of the pressure-induced changes to both the structures and optoelectronic properties. 36,37,45 However, this review will focus on experimental high-pressure effects. Recent improvements in high-pressure experimental platforms have enabled more precise control over pressure conditions and enhanced optical accessibility within diamond anvil cells, allowing for real-time, multimodal measurements. These advancements facilitate a deeper understanding of the correlation between structural changes and optoelectronic properties, ultimately guiding the rational design of pressure-tunable 2D perovskite materials.

Figure 3. High-pressure setup and instrumentation. (a) Schematic of DAC. Reproduced from ref. 63 with permission from IntechOpen, copyright 2011. (b) Raman set up. Reproduced from ref. 64

Open Access Article. Published on 28 Mphalane 2025. Downloaded on 2025-11-04 19:45:23

3. Pressure-Induced Phase Transitions in 2D Perovskites

The layered nature of 2D hybrid organic-inorganic perovskites (HOIPs) gives rise to complex and highly tunable structural responses under hydrostatic pressure. Compared to their 3D counterparts, 2D HOIPs exhibit more diverse and pressure-accessible polymorphic behavior due to their soft organic interlayers and relatively weak van der Waals bonding.^{6,13} This section summarizes representative high-pressure phase transitions in selected 2D HOIPs, emphasizing how such transitions differ in RP and DJ-type systems, and how spacer flexibility can influence phase stability and transformation pathways and how the type of spacer can also lead to the occurrence of rare phenomena such as negative linear compressibility (NLC) and decreased octahedral distortion.

3.1. RP-type 2D perovskites

Pressure-induced phase transitions have been observed at low pressures (typically <5 GPa) in most RP-type 2D HOIPs. For example, (BA)₂PbI₄ (BA = butylammonium), because of the soft organic spacers and van der Waals gaps, undergoes rapid and sequential structural phase transitions from its orthorhombic *Pbca* phase at ambient pressure. ^{21,22} Yin et al. reported three phase transitions starting with the room temperature (RT) to low temperature (LT) *Pbca* phase at 0.1 GPa, followed by a LT + HP (monoclinic $P2_1/a$) phase at ~ 1.6 GPa, and finally completed transition to the monoclinic $P2_1/a$ HP phase ~ 5.2 GPa and amorphization above ~6 GPa, highlighting the intrinsic flexibility and pressure sensitivity of RP structures (Figure 4a and Figure 4b).²¹ Similarly, Yuan et al. also reported a sequence of phase transitions beginning with an isostructural phase transition observed around 0.17 GPa evidenced by the appearance of several new peaks in the XRD spectra and the abrupt shift of the first reflection (Figure 4c) resulting in a more staggered octahedra along with rearrangement of the BA organic cations (Figure 4d).²² The appearance of further reflections around 2 GPa (Figure 4c) indicates a second phase transition likely corresponding to an orthorhombic $(Pbca) \rightarrow$ monoclinic (P2/a) transition resulting in a disordered structure with uncorrugated inorganic layers (Figure 4d).²² These transitions are driven by a combination of

Open Access Article. Published on 28 Mphalane 2025. Downloaded on 2025-11-04 19:45:23

increased octahedral tilting, the disruption of long-range order under compression, and the flexibility and bulkiness of the BA spacer cation, which facilitates layer sliding.²² In contrast, (PEA)₂PbI₄ (PEA = phenethylammonium) with a rigid PEA organic spacer has been shown to undergo more subtle transition.^{19,51} Liu et al. reported considerable broadening of the XRD peaks beyond 10.2 GPa, indicating distortion of the crystal lattice under high pressure (Figure 5a), whilst the equatorial and axial Pb-I bond lengths were found to contract significantly upon compression from 0 to 6 GPa (Figure 5b) and further confirmed by the theoretical crystal structures at 0 and 4 GPa, respectively, which underlined significant out-of-plane squeezing of the organic part.¹⁹ Thus, these results suggest anisotropic compression and a lack of distortion between 0 to 6 GPa.¹⁹ In another study, Guo et al reported that (PEA)₂PbI₄ maintains its layered orthorhombic symmetry until ~5.8 GPa, followed by a subtle order—disorder transition evidenced by the observed broadening in the XRD spectra (Figure 5c) involving realignment of phenyl rings resulting in a transition from AB (perpendicular) to AA (parallel) arrangement of the PEA spacer cations (Figure 5d).⁵¹

Figure 4. Sequential phase transitions of RP-type (BA)₂PbI₄. (a) In situ XRD spectra upon compression to 7.6 GPa and (b) schematic of crystal structures in the RT, LT, and HP phases. Reproduced from ref. 21 with permission from American Chemical Society, copyright 2018. (c) XRD spectra upon compression to 25.5 GPa and (d) schematic of change in crystal structure from ambient pressure to 2.0 GPa. Reproduced from ref. 22 with permission from Wiley-VCH GmbH, copyright 2019.

Figure 5. Subtle structural transition of RP-type (PEA)₂PbI₄. (a) XRD spectra upon compression to 19.9 GPa and (b) Pb-I bond lengths as functions of pressure. Reproduced from ref. 19 with permission from American Association for the Advancement of Science, copyright 2019. (c) XRD spectra upon compression to 9.2 GPa and (d) Crystal structures showing both AB and AA stacking arrangements. Reproduced from ref. 51 with permission from American Chemical Society, copyright 2019.

3.2. DJ-type 2D perovskites

DJ systems, which incorporate more rigid organic spacers, undergo more subtle phase transitions which are often isostructural in nature such as those observed in (2meptH₂)PbCl₄ (2mept = 2-methyl-1,5-diaminopentane) (Figure 6a),³⁴ and (API)PbBr₄ (API = N-(3-aminopropyl)imidazole) (Figure 6b).⁴⁶ In (2meptH₂)PbCl₄ only broadening of the ADXRD peaks is observed upon compression (Figure 6c) along with significant unit cell volume collapse at 2.1 GPa (Figure 6d),

suggesting an isostructural phase transition at 2.1 GPa.³⁴ Similarly, for (API)PbBr₄ again only broadening of the XRD peaks is observed upon compression (Figure 6e), once again suggesting an isostructural phase transition around 2.7 GPa and evidenced by the appearance of a new peak in the Raman spectra beyond 2.7 GPa (Figure 6f).⁴⁶ Furthermore, an abrupt decrease in both the cell parameters (Figure 6g) and unit cell volume is observed around 2.7 GPa (Figure 6h), providing further evidence of the isostructural phase transition around 2.7 GPa.⁴⁶ DJ systems can also resist pressure-induced reorganization until much higher pressures. When deformation finally occurs, irreversible transitions to disordered or amorphous states can occur, such as those observed in 3AMP-based compounds (3AMP = 3-(aminomethyl) piperidinium).²⁵ Kong et al. observed monotonic shifts of the diffraction peaks to higher 2θ angles followed by structural collapse and irreversible amorphization at higher pressures.²⁵ It should be noted that the pressure-driven amorphization was a progressive process rather than a sharp transition.²⁵

Figure 6. Pressure-induced structural changes in DJ-type 2D HOIPs with rigid spacers. (a) Crystal structure at ambient pressure of (2meptH₂)PbCl₄. Reproduced from ref. 34 with permission from Royal Society of Chemistry, copyright 2023. (b) Crystal structure at ambient pressure of (API)PbBr₄. Reproduced from ref. 46 with permission from Wiley-VCH GmbH, copyright 2024. (c) and (d) In situ ADXRD spectra upon compression to 30.8 GPa and unit cell volume as a function of pressure of (2meptH₂)PbCl₄. Reproduced from ref. 34 with permission from Royal Society of Chemistry, copyright 2023. (e)–(h) In situ XRD spectra upon compression to 10.6 GPa, Raman spectra upon compression to 8.2 GPa, normalized unit cell parameters as functions of pressure, and unit cell volume as a function of pressure of (API)PbBr₄. Reproduced from ref. 46 with permission from Wiley-VCH GmbH, copyright 2024.

3.3. Effects of spacer geometry and rigidity

Spacer geometry and rigidity can also play a central role in pressure response. Soft spacers such as BA and CMA (cyclohexylmethylammonium) offer greater flexibility and thus allow for more prominent pressure responses leading to sequential phase transitions previously discussed for $(BA)_2PbI_4$, 21,22 and significant negative linear compressibility (NLC) in $(CMA)_2PbI_4$ as discussed later. In contrast, systems with rigid π -conjugated spacers such as PEA, have been found to restrict lattice adjustment and can induce octahedral distortions under compression. For instance, octahedral distortion exhibited in RP systems incorporating PEA, i.e., $(PEA)_2PbX_4$ (X = I, Br, Cl), often leads to deformation of the Pb-X framework as observed in $(PEA)_2PbI_4$, and $(PEA)_2PbI_4$. Similarly, Liu et al. observed a greater resistance to compression for $(PEA)_2PbI_4$, 19

while Gao et al. observed broad band XRD peaks upon compression attributed to deformation of the PbI₄ skeleton.⁵¹

However, rigid spacers can also induce more complex phase diagrams. For example, triazolium-based perovskites exhibit four distinct polymorphs under pressure, as observed in Tz_2PbBr_4 (Figure 7a) which was found to undergo three separate phase transitions evidenced by significant changes in the Raman spectra upon compression (Figure 7b).⁵⁶ Firstly, the splitting of the δC –H, δNCN and γN –H modes at 1251.0, 949.3, and 722.3 cm⁻¹ is observed above 2.4 GPa (phase II), which is then followed by further significant changes at 6 GPa where two high-pressure phases (phase II and phase III) coexist, and lastly weak changes of the Raman bands in the lattice mode region are observed up to 8 GPa followed by significant broadening above 8.5 GPa indicating a third phase transition (phase III to phase IV) between 8 and 8.5 GPa.⁵⁶

Frequently, isostructural phase transitions have been observed in 2D HOIPs with both soft and rigid spacers. For example, an isostructural phase transition was observed in soft RP-type (CMA)₂PbI₄ (CMA = cyclohexylmethylammonium) (Figure 7c) evidenced by the lack of significant changes in the XRD spectra (Figure 7d).³⁶ Similarly, an isostructural phase transition was also observed in rigid DJ-type DPDAPbI₄ (DPDA = N,N-dimethylphenylene-*p*-diammonium) (Figure 7e), again evidenced by a lack of significant changes in the XRD spectra and further confirmed by a discontinuity in the experimental Rietveld refined unit cell volume around 1.5 GPa (Figure 7f).⁴⁵

For both RP and DJ systems, when compression pressure is sufficiently high, pressure-induced amorphization is often observed but with different transition pressures. In general, RP systems with soft spacers exhibit a higher threshold for amorphization, typically in the range of 5-10 GPa, whereas DJ systems have a relatively lower amorphization threshold (2-3 GPa), often preceded by an order-disorder transition. The different amorphization thresholds between the two systems are associated with the spacer rigidity and its interplay with the inorganic octahedra, such that external stress is mitigated by the spacer component of RP systems whereas the inorganic moiety of the DJ systems act as the primary responder to compression. Nonetheless, the amorphization threshold compared, to that for pure inorganic perovskites such as CsPbBr₃ (typically > 20 GPa) is much

Journal of Materials Chemistry A Accepted Manuscript

lower due to the lack of organic spacer as disorder precursor and contributor. Correspondingly, the reversibility of the amorphization-recrystallization cycles can be rationalized by examining several factors including spacer rigidity and flexibility, layer thickness, hydrogen bonding character, and experimental conditions. Typically, both RP and DJ-type 2D HOIPs were found to exhibit either full or partial reversibility upon decompression, whereas irreversible amorphization or disordering is observed in inorganic perovskites such as CsPbBr₃. These findings highlight how spacer rigidity and conformational freedom modulate both the mechanical anisotropy and phase stability of 2D HOIPs, offering a pathway to tailor their pressure resilience through molecular design.

Figure 7. Space-influenced pressure-induced structural changes of 2D HOIPs. (a) Crystal structure of Tz₂PbBr₄ at ambient pressure and (b) representative Raman spectra of Tz₂PbBr₄ in the 200–40 cm⁻¹ range. Reproduced from ref. 56 with permission from Royal Society of Chemistry, copyright 2024. (c) Crystal structure of (CMA)₂PbI₄ at ambient pressure and (d) ADXRD spectra upon compression at selected pressures. Reproduced from ref. 36 with permission from American Chemical Society, copyright 2023. (e) Crystal structure of DPDAPbI₄ at ambient pressure and (f) normalized unit cell volume as a function of pressure. Reproduced from ref. 45 with permission from Wiley-VCH GmbH, copyright 2025.

3.4. Pressure-induced rare phenomena

Furthermore, the type of organic spacer (either soft or rigid) can also result in the rare or uncommon pressure-induced phenomena in 2D HOIPs. For example, RP-type (CMA)₂PbI₄ exhibits a prominent negative linear compressibility (NLC) is observed between 1.1 and 1.2 GPa evidenced by the increase in the b parameter (Figure 8a), which is in stark contrast to both (PEA)₂PbI₄ and (BA)₂PbI₄.³⁶ The observed NLC is believed to result from possible rotation of the CMA ring along the a-axis thus enhancing the stacking efficiency but subsequently causing a slight expansion of the b-axis (Figure 8b).³⁶ Such NLC behavior resulting in enhanced anisotropic pressure-tuned stacking efficiency involving a soft and highly flexible spacer cation has not been previously observed in other 2D HOIPs.³⁶ In contrast, the rigidity of the DPDA spacer in DJ-type DPDAPbI₄ plays a significant role in the pressure behavior, in particular distortion analysis underlined the uncommon phenomena of reduced octahedral distortion until 1 GPa followed by an abrupt enhancement between 1-2 GPa (Figure 9a) with the initial decrease believed to be caused by the deep insertion of the DPDA spacer cation into the PbI₆ octahedral pockets resulting in decreased penetration depth upon compression (Figure 9b).⁴⁵

Figure 8. Pressure-induced rare phenomena in $(CMA)_2PbI_4$. (a) Normalized unit cell parameters and unit cell volume as functions of pressure showing NLC along the *b* direction and (b) possible rotation of the CMA ring (shown by red arrow) along the *a*-axis. Reproduced from ref. 36 with permission from American Chemical Society, copyright 2023.

Figure 9. Pressure-induced uncommon phenomena in DPDAPbI₄. (a) bond length distortion as a function of pressure showing relaxation of octahedral distortion at low pressure and (b) penetration depth of DPDA spacer as a function of pressure. Reproduced from ref. 45 with permission from Wiley-VCH GmbH, copyright 2025.

Overall, pressure is a highly effective method for modifying the structures of 2D HOIPs in particular by inducing phase transitions, octahedral tilting and distortion, and amorphization. The geometry and rigidity of the organic spacer cations can not only influence the pressure response but can also at times result in rare phenomena. Table 1 summarizes key structural transitions reported in representative 2D HOIPs under compression.

Table 1. Pressure-induced structural phase transitions in representative 2D HOIPs.

This table summarizes key high-pressure structural responses of 2D perovskites, classified by phase type (RP or DJ), spacer rigidity, and inorganic composition. Phase transitions typically occur at relatively low pressures (<5 GPa), reflecting the structural softness of 2D HOIPs compared to their 3D counterparts. RP systems with soft organic spacers (e.g., BA, CMA) undergo sequential phase transitions and amorphization, while those with rigid aromatic spacers (e.g., PEA) exhibit subtle or order–disorder transitions. DJ systems, stabilized by bifunctional spacers, generally show higher resistance to compression, often undergoing isostructural transitions or gradual amorphization at elevated pressures. The table highlights the influence of spacer geometry and connectivity on compressibility and phase stability.

4. Tuning Optoelectronic Properties with Pressure

Whilst high pressure has been shown to be highly effective at inducing structural modifications through phase transitions primarily caused by changes in the octahedral distortion and interlayer interactions, high pressure has also been shown to effectively tune the optoelectronic properties (i.e. PL emissions and bandgaps) of 2D HOIPs thus making high pressure a promising method for tuning such properties to make them ideal candidates for several applications, in particular solar cells and light emitting diodes. In this section the pressure-induced optoelectronic properties of 2D HOIPs are discussed showing how pressure can cause changes to the bandgaps, PL emissions, and

charge carrier lifetimes, whilst also enabling metastable states with enhanced properties in certain compounds.

4.1. General trend of bandgap evolution

This article is licensed under a Creative Commons Attribution-NonCommercial 3.0 Unported Licence.

Open Access Article. Published on 28 Mphalane 2025. Downloaded on 2025-11-04 19:45:23

One of the most prominent pressure responses in 2D HOIPs is the modulation of the bandgap. Several bandgap trends can occur upon compression with the most common one being a gradual redshift of the absorption edge (gradual bandgap narrowing) upon compression which has been observed in several previously studied 2D HOIPs. Ratté et al. observed a continuous gradual redshift of the absorption edge until 15.23 GPa (Figure 10a) corresponding to a significant bandgap reduction from 2.33 to 1.89 eV ($\Delta E_g = 0.44$ eV) upon compression to 11.3 GPa (Figure 10b) for soft RP-type (CMA)₂PbI₄, in good agreement with the DFT calculated bandgap values, and the bandgap was found to remain direct throughout the compression process.³⁶ The authors attributed the monotonic bandgap narrowing and constant direct nature to anisotropic contraction of the PbI₆ octahedra as opposed to tilting evidenced by the compression of the axial and equatorial Pb-I bond lengths with the latter showing greater compression at high pressure.³⁶ Similarly, Kutty et al. also observed a gradual continuous redshift of the absorption edge upon compression beyond 6.87 GPa (Figure 10c) corresponding to a significant monotonic bandgap reduction from 2.26 to 1.87 eV $(\Delta E_g = 0.39 \text{ eV})$ upon compression to 8.84 GPa (Figure 10d) for rigid DJ-type DPDAPbI₄, again in excellent agreement with the DFT computations and once again the direct bandgap nature was maintained throughout compression. 45 However, unlike for (CMA)₂PbI₄, the monotonic bandgap reduction for DPDAPbI₄ was found to result from the strong correlation between the enhancement of both the N-H-I hydrogen bonding interactions and PbI₆ octahedral distortion at low pressure (> 2 GPa) whilst at higher pressure the rigidity of the DPDA spacer and overall electronic configurations collectively determined the optoelectronic properties.⁴⁵

Similar strong correlation between the hydrogen bonding interactions and bandgap evolution were observed in a rigid RP-type system, (PMA)₂PbI₄ where (PMA = phenylmethylammonium), with the enhancement of the hydrogen bonding interactions inducing distortion of the PbI₆ octahedra and in turn a significant bandgap narrowing from 2.19 to 1.26 eV ($\Delta E_g = 0.93$ eV).²⁹ Interestingly, Gao et al. observed bandgap narrowing from 2.26 to 1.83 eV ($\Delta E_g = 0.43$ eV) upon compression to 5.8 GPa in another rigid RP-type system, (PEA)₂PbI₄, followed an abrupt jump to 1.95 eV and

Open Access Article. Published on 28 Mphalane 2025. Downloaded on 2025-11-04 19:45:23.

a direct-to-indirect bandgap transition attributed to the AB to AA stacking arrangement phase transition discussed previously.⁵¹ These results not only underline how the type of organic spacer can influence the bandgap behavior at high pressure but as observed in (PEA)₂PbI₄ pressure can also result in deviations away from the general bandgap trends as discussed later.

Overall, all 2D HOIPs, including both RP and DJ types, display universal pressure-induced bandgap narrowing albeit to different extent. Remarkably, compared to classical inorganic 2D materials such as MoS_2 , the absolute value of pressure-induced bandgap reduction in 2D HOIPs is exceptionally large, given that most inorganic 2D materials already have low initial bandgaps (e.g., < 1.5 eV) and often undergo a transition to metallic state at moderate pressures. As summarized in Table 3 below, while the general tunability for 2D HOIPs is $\Delta E_g \approx 0.5$ eV over a 10 GPa range on average, select systems exhibit much greater bandgap reductions— e.g., 1.33 eV and 0.93 eV observed for RP-type (BA)₂PbI₄ and (PMA)₂PbI₄, respectively.^{22,29} Moreover, compared to DJ type, RP type HOIPs generally show more prominent bandgap reduction, especially with soft spacers due to the larger compressible-pressure range, although some RP systems with rigid spacers may display non-monotonic trends as illustrated below.

Figure 10. Pressure-induced optical absorbance behavior of 2D HOIPs with differing organic spacers. (a) In situ UV-Vis absorption spectra upon compression to 15.23 GPa and (b) bandgap as a function of pressure for (CMA)₂PbI₄. Reproduced from ref. 36 with permission from American Chemical Society, copyright 2023. (c) In situ UV-Vis absorption spectra upon compression to 6.87 GPa and (d) bandgap as a function of pressure for DPDAPbI₄. Reproduced from ref. 45 with permission from Wiley-VCH GmbH, copyright 2025.

4.2. Beyond the Norm: Blueshifts and Non-Monotonic Trends

One such unusual and intriguing pressure-induced bandgap trend is an initial blueshift of the absorption edge (bandgap widening) at low pressure due to lattice contraction and increased octahedral tilting, which reduces electronic coupling and narrows bandwidths, whilst at higher pressure the bond lengths shorten and Pb–X–Pb bond angles approach linearity, enhancing orbital overlap and resulting in a redshift of the absorption edge (bandgap narrowing). Such a trend has been observed previously in (BA)₂PbI₄.^{21,22} Yin et al. observed piezochromic transitions upon compression to 10 GPa (Figure 11a) evidenced by an initial blueshift of the absorbance peak upon compression to 0.4 GPa followed by a continuous redshift upon further compression and the

emergence of a second peak beyond 1.9 GPa whilst broadening beyond 5 GPa indicating the onset of amorphization (Figure 11b).²¹ Theoretical studies indicated a decrease in the Pb–I–Pb bond angle from 150.2° to 144.9° along with an increase in the average equatorial Pb-I bond length from 3.09 Å to ~3.14 Å at 0.4 GPa, thus leading to diminished Pb-I orbital overlap and the subsequent initial blueshift of the absorbance peak.²¹ Further compression resulted in the expected opposite trend, the bond angle and average equatorial bond length increased and decreased back to 150.5° and 3.09 Å, respectively leading to the continuous redshift of the main absorbance peak and the second peak beyond 1.9 GPa (Figure 11b).²¹ Similarly, Yuan et al. also observed an initial abrupt blueshift of the absorption edge (Figure 11c) and subsequent bandgap widening from 2.28 to 2.37 eV (Figure 10d) upon compression to 0.22 GPa followed by a continuous redshift (Figure 11c) and bandgap narrowing to 0.95 eV at around 35 GPa (Figure 11d).²² Yuan et al. also observed new absorption edges upon compression to 2.2 and 13.1 GPa (Figure 11c) which they attributed to second and third phase transitions with increased PbI₆ octahedral tilting leading to the initial bandgap widening and subsequent decreased tilting and Pb-I bond length shortening resulting in the gradual bandgap narrowing (Figure 11d).²²

Figure 11. Pressure-induced optical absorbance behavior of (BA)₂PbI₄. (a) Optical images at selected pressures illustrating piezochromism and (b) In situ UV-Vis absorption spectra. Reproduced from ref. 21 with permission from American Chemical Society, copyright 2018. (c) In situ UV-Vis absorption spectra upon compression to 39.7 GPa and (d) bandgap as a function of pressure. Reproduced from ref. 22 with permission from Wiley-VCH GmbH, copyright 2019.

Another unusual pressure-induced bandgap trend that has been observed is that of a continuous redshift of the absorption edge (bandgap narrowing) followed by an abrupt blueshift (bandgap widening) and finally a re-redshift (re-reduction). Such pressure-induced bandgap behavior has been previously exhibited in (PEA)₂PbBr₄.^{27,52} Ren et al. observed a prominent redshift of the absorption edge upon initial compression to 10 GPa (significant bandgap narrowing from 2.99 to ~ 2.5 eV) followed by an abrupt blueshift (bandgap widening) between 10–28.4 GPa and subsequent re-redshift (re-reduction) between 28.4–48.2 GPa (Figure 12a and 12b).²⁷ Once again the first redshift was attributed to lattice contraction of the crystallized sample while abrupt blueshift was attributed to amorphization causing the distorted PbBr₆ octahedra with subsequent contraction of the disordered lattice resulting in the re-redshift.²⁷ Zhang et al. also observed a significant redshift of the absorption edge upon compression to ~ 12 GPa followed by an abrupt

blueshift until ~ 15 GPa and finally a gradual re-redshift until 28.4 GPa (Figure 12c) resulting in a significant bandgap narrowing from 2.96 to 2.46 eV followed by a slight bandgap widening and gradual re-reduction (Figure 12d).⁵² The initial redshift and significant bandgap reduction was attributed to the soft oriented organic cation layer causing enhanced orbital overlap of Pb s and Br p states.⁵² The abrupt blueshift and subsequent bandgap widening was attributed to PbBr₆ octahedral distortion leading to reduced compressibility and in turn decreased metal-halide orbital coupling.⁵² Finally, the re-redshift and re-reduction of the bandgap was believed to result from the competition of the compression effect with the interlayer bond contraction and lattice distortion.⁵²

Figure 12. Pressure-induced optical absorbance behavior of (PEA)₂PbBr₄. (a) In situ UV-Vis absorption spectra upon compression to 48.2 GPa and (b) bandgap as a function of pressure. Reproduced from ref. 27 with permission from AIP Publishing, copyright 2020. (c) In situ UV-Vis absorption spectra upon compression to 28.4 GPa and (d) bandgap as a function of pressure. Reproduced from ref. 52 with permission from Wiley-VCH GmbH, copyright 2018.

These diverse pressure-induced bandgap behaviors—monotonic, non-monotonic, or flattened—can be consistently rationalized using the competing effects of bond contraction and octahedral tilting. In soft-spacer (e.g. long alkylammonium chains) RP systems, flexible organic layers accommodate pressure through lattice compression, allowing bond shortening to dominate and yielding continuous bandgap narrowing. In contrast, rigid DJ systems where the organic layer is more rigid or tightly bound (e.g. diammonium linkers or aromatic cations that lock adjacent layers together), often resist direct compression, leading to enhanced octahedral tilting or distortion at lower pressures, which can counteract or even reverse the redshift, leading to the bandgap widening. This framework also explains the non-monotonic trends observed in certain systems: an initial redshift arises from bond contraction, followed by a blueshift or bandgap plateau as tilting becomes more pronounced beyond a structural crossover pressure. Recognizing this mechanistic balance provides a unified lens through which to interpret the system-dependent optical responses seen across 2D HOIP families under compression.

4.3. Photoluminescence: Enhancement and Quenching Pathways

Along with modulation of the bandgap, pressure can also, at times, increase photoluminescence (PL) intensity in many 2D perovskites. This PL enhancement is often attributed to the suppression of non-radiative recombination pathways, such as trap-assisted processes, as pressure passivates

defects and reduces lattice strain. Such suppression of trapped states has been previously observed in GA-based (GA = guanidinium) 2D HOIPs. 50,53 For example, Chen et al. observed a 5-fold PL enhancement upon compression to 1.3 GPa (Figure 13a) followed by a gradual decrease until quenching at 7 GPa in (GA)(MA)₂Pb₂I₇ (Figure 13b).⁵⁰ Interestingly, the PL peak was found to redshift initially followed by an abrupt blueshift until quenching (Figure 13a and 13b).⁵⁰ The PL enhancement was believed to result from confinement of the charge carriers due to volume contraction upon compression thus leading to increased exciton binding energy, while the gradual decrease in intensity was believed to result from the suppression effect in the emission process.⁵⁰ Similarly, Guo et al. observed a sharp 12-fold PL enhancement upon compression to 1.59 GPa followed by a gradual decrease until eventual quenching at 9.48 GPa in (HA)₂(GA)Pb₂I₇ (Figure 13c).⁵³ Upon fitting the PL spectra, the authors observed a strong contribution to the PL emission from trapped states at ambient pressure which then gradually decreases upon compression until 1.59 GPa where the contribution is fully from free excitons (FE) (Figure 13d).⁵³ More significantly, Guo et al. reported an extraordinary 72-fold PL enhancement for RP-type (BA)₂(GA)Pb₂I₇ upon compression to 2.1 GPa, which was attributed to the suppression of exciton trapping.³⁹ Thus, it is believed that that PL enhancement in general is associated with the suppression of carrier trapping due to reduced distortion of the Pb-I sublattice leading a decrease in the energy barrier between the FE and trapped states.⁵³

Figure 13. Pressure-induced PL enhancement of GA-based 2D HOIPs. (a) and (b) In situ PL spectra upon compression to 1.3 and 7.0 GPa respectively for (GA)(MA)₂Pb₂I₇. Reproduced from ref. 50 with permission from Royal Society of Chemistry, copyright 2019. (c) and (d) In situ PL spectra upon compression to 9.48 GPa and fitted PL spectra at selected pressures for (HA)₂(GA)Pb₂I₇. Reproduced from ref. 53 with permission from Wiley-VCH GmbH, copyright 2020.

In comparison to the RP-type and ACI-type systems, DJ-type 2D HOIPs tend to exhibit less prominent PL enhancements upon compression. For example, the PL intensity for DPDAPbI₄ exhibits a slightly more than twofold enhancement upon compression to 1.5 GPa followed by a gradual decrease until eventual quenching at 5.6 GPa.⁴⁵ For (API)PbBr₄, the FE PL peak shows an approximately fivefold enhancement upon compression to 2.7 GPa followed by a gradual decrease until quenching at around 6 GPa.⁴⁶ Furthermore, all the observed PL enhancements were in excellent agreement with the corresponding isostructural phase transitions.^{45,46} Overall, it appears

Open Access Article. Published on 28 Mphalane 2025. Downloaded on 2025-11-04 19:45:23

that all RP-, DJ- and ACI-type 2D HOIPs undergo initial pressure-induced PL enhancements followed by quenching, although the associated PL mechanisms may differ, as discussed below.

4.4. From Free Excitons to STEs: Pressure-Driven PL Mechanisms

Notably, pressure not only tunes PL intensity but can also qualitatively change its nature. In several lead-based RP perovskites, initial PL emission is associated with free excitons followed by broadband emission emerging under moderate pressure (~ 4–6 GPa), associated with self-trapped excitons (STEs). Such behavior has been previously exhibited in RP-type (PEA)₂PbBr₄, where Zhang et al. also observed a gradual redshift and intensity decrease of the initial FE PL peak and the emergence of the broadband STE peak around 4 GPa in RP-type (PEA)₂PbBr₄ (Figure 14a).⁵² The presence of the STE peak was attributed to increased lattice distortion upon compression due to localization of charge carriers leading to stable STEs, while the lack of lattice distortion at low pressure means stable STEs cannot form, thus only the FE peak is visible (Figure 14a).⁵² Similarly, Maczka et al. observed an initial linear redshift of the FE PL peak upon compression to ~ 2 GPa followed by a less pronounced redshift between 2–6 GPa and the emergence of the broadband STE PL peak at 4.42 GPa in RP-type Tz₂PbBr₄ (Figure 14b).⁵⁶ The redshift until ~ 2 GPa was attributed to substantial shortening of the Pb–Br bonds while the less pronounced shift between 2–6 GPa was attributed to tilting and distortion of the PbBr₆ octahedra, consistent with the first pressure-induced phase transition around 2 GPa.⁵⁶ The lack of significant shift of FE peak between 6–8 GPa but continued intensity increase was attributed to the compensation of the Pb-Br bond length shortening by the octahedral tilting and distortion, consistent with the second pressure-induced phase transition around 6 GPa, and finally an abrupt blueshift and decreased intensity beyond 8 GPa of both the FE and STE peaks is observed attributed to stronger pressure-induced octahedral tilting and distortion in comparison to Pb-Br bond length shortening, consistent with the third and final pressure-induced phase transition between 8 and 8.5 GPa.⁵⁶

Figure 14. Pressure-induced change in PL nature of RP-type 2D HOIPs. (a) In situ PL spectra upon compression to 15.6 GPa of (PEA)₂PbBr₄. Reproduced from ref. 52 with permission from Wiley-VCH GmbH, copyright 2018. (b) In situ PL spectra upon compression to 13.4 GPa of Tz₂PbBr₄. Reproduced from ref. 56 with permission from Royal Society of Chemistry, copyright 2024.

Building on this mechanistic picture, Guo et al. presented a concise structure–PL map that links how the inorganic sheets and organic spacers accommodate compression to the balance between free-exciton and self-trapped emission for RP-type HOIPs.³⁹ They showed that pressure which primarily reduces intralayer disorder while tightening interlayer coupling tends to suppress trap-assisted or STE-like features and steer the spectra toward brighter, more symmetric FE emission; conversely, when compression is absorbed mainly through enhanced octahedral tilting or layer misregistry, STE signatures are stabilized and can overtake FE. Viewed this way, the appearance, crossover, or quenching of broad STE bands across RP families—and the possibility of reproducing FE-dominated emission by chemically emulating the pressure-optimized packing through spacer choice—follow from the same structural lever, offering a transferable design rule for tuning emissive pathways under pressure.

DJ-type 2D HOIPs also exhibit both FE and STE contributions, but their pressure evolution often contrasts with RP analogues. In (API)PbBr₄, an initially STE-dominated spectrum narrows into an FE-like line under modest compression as enhanced carrier delocalization suppresses STE formation. 46 Conversely, DPDAPbI₄ shows a transient broadening and asymmetry at low compression consistent with STE admixture, followed by recovery of a symmetric, FE-dominated profile as further pressure reduces octahedral distortion.⁴⁵ Across these DJ examples, PL enhancement at increasing pressure is primarily associated with the FE channel, 45 while STE features are typically stabilized only within a limited low-to-intermediate pressure window when tilting or interlayer misregistry is prominent—opposite to many RP cases where STE bands emerge and intensify at moderate pressures. This behavior reflects stronger through-layer connectivity in DJs (bifunctional spacers and robust hydrogen bonding) that constrains layer sliding and promotes pressure-induced delocalization, broadening the regime where FE emission outcompetes STE; at sufficiently high loads, however, accumulated disorder and non-radiative pathways ultimately quench luminescence. The precise crossover pressures remain spacerand composition-dependent. 45,46

4.5. Charge-Carrier Lifetimes: Pressure as a Trap Suppressor

Pressure can also modulate charge-carrier lifetimes, which can be measured using time-resolved PL measurements (TRPL), where carrier lifetimes typically increase as non-radiative pathways are eliminated under pressure and then collapse when amorphization or non-emissive transitions dominate. For example, Yin et al. found that in (BA)₂PbI₄, the lifetime increased from 150 to 190 ps upon compression to 0.4 GPa, with the STE (slow decay) lifetime undergoing a significant increase from 320 to 440 ps (Figure 15a and 15b) attributed to an increase of trapped excitons by the distorted PbI₄²⁻ lattices.²¹ Upon further compression to 2.3 GPa, the lifetime decreased to 53 ps with the STE lifetime decreasing to 148 ps (Figure 15c) as non-radiative recombination increased resulting from increased defects due to the onset of amorphization.²¹ Similarly, in (2meptH₂)PbCl₄ the average carrier lifetime exhibits a significant increase until 10.2 GPa, again associated with increased radiative recombination resulting in PL enhancement, followed by a gradual decrease, again associated with increased non-radiative recombination resulting in PL quenching (Figure 15d).³⁴

Figure 15. Pressure-induced charge carrier lifetimes of 2D HOIPs. (a), (b), and (c) TRPL spectra of (BA)₂PbI₄ at 0, 0.4, and 2.3 GPa, respectively. Reproduced from ref. 21 with permission from American Chemical Society, copyright 2018. (d) Average PL lifetime as a function of pressure of (2meptH₂)PbCl₄. Reproduced from ref. 34 with permission from Royal Society of Chemistry, copyright 2023.

Furthermore, in certain cases the structural rearrangements persist after pressure release, resulting in metastable phases with enhanced optoelectronic properties. For example, structural amorphization upon compression followed by recrystallization upon decompression in (BA)₂(MA)₂Pb₃I₁₀ resulted in metastable states which exhibited significant bandgap narrowing of 8.2%.⁴⁷ Metastable states have also been observed in GA-based compounds, for example in (GA)(MA)₂Pb₂I₇ decompression from 25.1 GPa resulted in a colour change from dark red to black and a bandgap decrease from 2.00 (pre-compression) to 1.79 eV (post-decompression), indicating irreversible pressure behavior ideal for practical applications.⁵⁰ In (HA)₂(GA)Pb₂I₇ decompression until 1.5 GPa results in significant PL enhancement via laser irradiation accompanied by a yellow to orange colour change which is retained at ambient pressure and exhibits PL enhancement of 100% compared to the original pre-compressed sample.⁵³ These observations raise the possibility of using pressure not only as a diagnostic tool but also for post-synthetic phase engineering, whilst

also suggesting a strategy for "strain-quenching" of pressure-induced states that could be useful for stabilizing materials for light emission or sensing.

Taken together, these results demonstrate that high pressure provides a robust route to tailor and even stabilize the optoelectronic properties of 2D HOIPs. The magnitude of modulation, reversibility, and emissive pathway depend strongly on dimensionality, spacer rigidity, interlayer coupling, and metal/halide identity. The strategic use of pressure can thus advance both the fundamental understanding and practical engineering of 2D perovskites. Table 2 summarizes the pressure-induced optoelectronic properties of representative 2D HOIPs.

Table 2. Summary of pressure-induced optoelectronic property changes in 2D HOIPs.

This table collates optical and electronic responses (bandgap shifts and PL modulation) under hydrostatic compression. Several general trends are evident: (i) soft-spacer RP systems often display monotonic bandgap narrowing with pressure, (ii) rigid-spacer systems can show abnormal behaviors such as initial blueshift or non-monotonic shifts, and (iii) DJ systems exhibit gradual tuning due to stronger interlayer interactions. Photoluminescence (PL) is frequently enhanced at low pressure due to defect passivation, followed by quenching at higher pressures. Notably, broadband self-trapped exciton (STE) emission and direct-to-indirect bandgap transitions have been observed in select systems, highlighting pressure as a versatile tuning parameter.

5. Lead vs Lead-Free: Contrasting Pressure Responses

Two-dimensional (2D) perovskites based on lead halides have been extensively studied for their superior optoelectronic properties and tunability under hydrostatic pressure. However, the toxic nature of Pb²⁺ and associated environmental concerns have motivated the development of lead-free alternatives. This section summarizes the pressure behavior of lead-free 2D perovskites, including Sn²⁺, Cu²⁺, Ge²⁺, and Bi³⁺ analogs, in terms of structural stability, bandgap evolution, PL response, and phase transition mechanisms.

A key advantage of lead-free 2D perovskites, in particular $\mathrm{Sn^{2+}}$ and $\mathrm{Cu^{2+}}$ -based ones, is the narrow bandgaps which allow for greater tuning under high pressure allowing for greater possibility for reaching the ideal Shockley-Queisser (SQ) limit, which states that at an optimal bandgap of 1.34 eV a maximum efficiency of 33.7% is achieved.^{67,68} Unfortunately, lead-free analogs often exhibit greater susceptibility to oxidation (e.g., $\mathrm{Sn^{2+}} \to \mathrm{Sn^{4+}}$), which can influence their high-pressure behavior and long-term stability. Despite this, certain Sn and Cu-based systems have demonstrated

similar or even enhanced phase transition pathways, PL enhancements, and bandgap shifts in comparison to their lead-based analogues. Bi³⁺-based 2D perovskites, with their larger tolerance for structural distortion, typically show broader bandgaps and more rigid frameworks, resulting in less pronounced PL modulation under pressure. Overall, while lead-free systems offer promising environmental advantages, their pressure responses are often more limited or require additional chemical tuning to match the performance and versatility of their lead-based counterparts.

5.1. Tin-Based Systems: High Tunability but Oxidation Challenges

Sn²⁺ is believed to be the most promising substitute for lead in the generation of 2D HOIPs owing to the highly favourable optical and electronic properties of Sn²⁺-based 2D HOIPs.⁶⁹ In particular, Sn²⁺-based 2D HOIPs with optical bandgaps between 1.2-1.4 eV have the potential to reach a power conversion efficiency (PCE) around 33%. 70 Furthermore, they also tend to exhibit similar or enhanced optical and electronic properties in comparison to their Pb-based analogues, including greater charge carrier mobilities and long-lived hot carriers.^{69,71,72} Unfortunately Sn²⁺-based 2D HOIPs suffer from lower chemical stability with Sn²⁺ readily oxidizing to Sn⁴⁺ under ambient conditions, 73 leading to poor reproducibility and efficiency and large doping concentrations. 74 Furthermore, high-pressure studies of Sn²⁺-based 2D HOIPs are very limited. A recent study by Kong et al. on an RP-type family, $(BA)_2(MA)_{n-1}Sn_nI_{3n+1}$ (n = 2-4), showed a significant bandgap reduction for the n = 2 sample from 1.65 to 1.17 eV upon compression to 6.2 GPa and significant enhancement of PL intensity until 1 GPa followed by a significant decrease and eventual quenching at 6.5 GPa (Figure 16).⁷⁵ Interestingly, all three samples exhibited similar patterns for both the PL emission and bandgap, with the PL intensity enhancing at low pressure before reducing and the bandgap exhibiting a significant redshift before a slight blueshift and re-redshift at high pressure (Figure 16). 75 Furthermore, the n = 2 sample exhibited the greatest the bandgap tunability $(\Delta E_g = 0.48 \text{ eV})$, much greater compared to that of the lead-analogue ($\Delta E_g = 0.15 \text{ eV}$), and lowest bulk modulus of 4.8 GPa indicating significant compressibility compared to its 3D Sn and 2D Pb counterparts. The bandgap and crystalline structure of the n = 2 sample were also found to be retained upon decompression from mild pressures.⁷⁵ This recent study underlines the strong possibility of Sn²⁺-based 2D HOIPs for achieving the desired SQ limit with considerable compressibility in comparison to the lead analogues. However, the limited high-pressure studies opens the door for more extensive studies to be conducted to fully understand the effects of high pressure on the structures and tuning of optoelectronic properties of Sn²⁺-based 2D HOIPs. These findings highlight the potential of Sn²⁺-based 2D HOIPs as viable alternatives for environmentally friendly optoelectronic applications—provided that oxidative degradation can be effectively mitigated. Continued advancements in encapsulation strategies and inert-atmosphere processing will be key to unlocking the full promise of these materials under high-pressure regimes.

Figure 16. Tuning of optoelectronic properties of (BA)₂(MA)_{n-1}Sn_nI_{3n+1} RP family. Absorption spectra upon compression for (a) (BA)₂(MA)Sn₂I₇, (b) (BA)₂(MA)₂Sn₃I₁₀, $(BA)_2(MA)_3Sn_4I_{13}$. PL spectra upon compression for (d) $(BA)_2(MA)Sn_2I_7$, (e) $(BA)_2(MA)_2Sn_3I_{10}$, and (f) (BA)₂(MA)₃Sn₄I₁₃. Bandgap as a function of pressure for (g) (BA)₂(MA)Sn₂I₇, (h) (BA)₂(MA)₂Sn₃I₁₀, and (i) (BA)₂(MA)₃Sn₄I₁₃. Reproduced from ref. 75 with permission from Wiley-VCH GmbH, copyright 2024.

5.2. Copper-Based Systems: Stability with Narrow Bandgaps

Another commonly studied alternative to lead in 2D HOIPs is copper, specifically Cu²⁺, which has emerged as a highly promising candidate due to its abundance, low cost, low environmental impact, and the unique electronic structure and excellent optoelectronic properties of Cu²⁺-based 2D HOIPs. 76,77 In contrast to tin, copper-based 2D HOIPs exhibit excellent stability mostly due to use of hydrophobic organic cations as spacers in between the inorganic layers, making them more moisture resistant in comparison to unstable 3D perovskites, and they are also less susceptible to oxidation under ambient conditions.^{77,78} Majority of Cu²⁺-based 2D HOIPs consist of Cu-Br or Cu-Cl octahedra, with Cu-Cl ones known for exhibiting thermochromism resulting from the lattice undergoing phase transitions resulting from temperature-dependent hydrogen bonding of cations. 77,78 More extensive high-pressure studies have been conducted on Cu²⁺-based 2D HOIPs compared to Sn²⁺-based ones, with those containing Cu-Br octahedra exhibiting greater potential for achieving the SQ limit compared to those with Cu-Cl octahedra due to the narrow bandgaps at ambient pressure. For example, Zahn et al. observed a significant bandgap reduction from 1.8 to 1.47 eV upon compression to 5 GPa (Figure 17a) in (PMA)₂CuBr₄ resulting from the deformation of the Cu-Br octahedrons due to rapid compression of the volume, but no significant phase transition.⁷⁹ Compression beyond 5 GPa results in a slight blueshift of the bandgap to 1.52 eV, attributed to pressure-induced tilting of the Cu-Br octahedron, after which the bandgap remains stable and 1.52 eV up to 29.1 GPa (Figure 17a), which is highly favourable for photovoltaic devices.⁷⁹ Similarly, Jaffe et al. observed a large bandgap reduction from 1.7 to 0.3 eV in

(EA)₂CuBr₄ upon compression to 65 GPa (Figure 17b). ⁸⁰ In contrast to (PMA)₂CuBr₄, (EA)₂CuBr₄ undergoes two distinct phase transitions first from the monoclinic *P*2₁/*c* structure at ambient pressure to orthorhombic *Cccm* upon compression to 2.6 GPa, resulting in octahedral tilting, followed by a second-order isostructural phase transition above 4 GPa, resulting in reduced compressibility. ⁸⁰ Li et al. also observed a substantial bandgap reduction in DABCuCl₄ from 2.44 to 2.05 eV upon compression to ~ 12 GPa along with an isostructural phase transition between ~ 6 and ~ 10 GPa (Figure 17c). ⁸¹ Zhou et al. observed an even greater bandgap reduction in (PEA)₂CuCl₄ from 2.93 to 1.77 eV upon compression to 20.37 GPa (Figure 17d), but similar to (PMA)₂CuBr₄ no significant phase transition was observed. ⁸² These findings help underline the greater probability for achieving the desired SQ limit in Cu-Br 2D HOIPs in comparison to Cu-Cl 2D HOIPs, and the lack of oxidation under ambient conditions and excellent stability makes Cu²⁺ a highly promising candidate to replace lead but further studies are likely required to deepen the understanding of both the structural evolution and bandgap behaviour under high pressure.

Figure 17. Pressure-induced bandgap behavior of Cu-based 2D HOIPs. (a) Bandgap as a function of pressure for (PMA)₂CuBr₄. Reproduced from ref. 79 with permission from Wiley-VCH GmbH, copyright 2022. (b) Bandgap as a function of pressure for (EA)₂CuBr₄. Reproduced from ref. 80 with permission from Wiley-VCH GmbH, copyright 2019. (c) Bandgap as a function of pressure for DABCuCl₄. Reproduced from ref. 81 with permission from American Chemical Society, copyright 2017. (d) Bandgap as a function of pressure for (PEA)₂CuCl₄. Reproduced from ref. 82 with permission from American Physical Society, copyright 2023.

5.3. Germanium-Based Systems: Underexplored but Promising

In contrast to tin and copper, germanium (Ge²⁺) has been studied far less as a potential alternative to lead mainly due to its rare abundance and high cost. However, germanium exhibits little toxicity and environmental damage in comparison to lead and a growing interest in Ge²⁺-based 2D HOIPs for various applications is anticipated in the coming years.⁸³ Unfortunately, like Sn²⁺ Ge²⁺ also shows a strong tendency to oxidize to Ge⁴⁺ under ambient conditions, but majority of the solutions to supress the oxidation proposed for Sn²⁺ can also be applied to Ge²⁺.⁸³ Furthermore, high-pressure studies on Ge²⁺-based 2D HOIPs are also highly scarce. In 2021 Morana et al. observed a reversible broadband PL peak in (DA)₂GeI₄ upon compression beyond 2.1 GPa, which reaches its maximum intensity around 3.7 GPa (Figure 18a), likely resulting from STE emission due to octahedral distortion.⁸⁴ An initial blueshift of the absorption edge is observed upon compression

to 0.2 GPa followed by a continuous redshift until 11.4 GPa leading to a significant reduction of the absorption edge from 2.28 to 1.64 eV (Figure 18b).⁸⁴ The onset of both the broadband PL emission and bandgap blueshift-redshift transition correlate excellently with the proposed phase transition from orthorhombic *Pbca* to monoclinic *P2*₁/*a* with a reduced *c*-axis between 0.56 and 2.20 GPa, evidenced by peak splitting in the XRD spectra at 2.20 GPa (Figure 18c) and discontinuity of the unit cell parameters around 0.56 GPa (Figure 18d).⁸⁴ Overall, this study once again indicates the strong probability for reaching the SQ limit in lead-free 2D HOIPs, however further, more in-depth studies are required to obtain a more solid foundation of the pressure response of Ge²⁺-based 2D HOIPs.

Figure 18. Behavior of (DA)₂GeI₄ under high pressure. (a) PL spectra upon compression, and (b) absorption edge as a function of pressure, (c) XRD spectra upon compression, and (d) unit cell parameters as functions of pressure. Reproduced from ref. 84 with permission from Elsevier, copyright 2022.

5.4. Bismuth-Based Systems: Robust but Optically Limited

Lastly, Bi³⁺-based double perovskites and layered compounds represent another lead-free direction. These systems are generally more rigid and exhibit wider, often indirect bandgaps. Under pressure, Bi-based compounds show mild bandgap narrowing, but less pronounced structural phase transitions compared to Pb or Sn systems. 54,85,86 For example, MA₃Bi₂Br₉ exhibited a phase transition between 4.3 and 5.0 GPa from trigonal $P\overline{3}m1$ to monoclinic $P2_1/a$ evidenced by the emergence of new peaks in the XRD spectra (Figure 19a). 85 A continuous redshift of the absorption edge (Figure 19b), resulting in a mild bandgap reduction of ~ 0.2 eV (Figure 20c), upon compression to 4.1 GPa was observed followed by a slight blueshift between 4.6 and 5.5 GPa and finally a re-redshift upon further compression to 10.4 GPa (Figure 19b), resulting in another mild bandgap reduction of ~ 0.1 eV (Figure 19c). 85 In comparison, Cs₃Bi₂I₆Cl₃ was found to exhibit a near constant bandgap upon compression to 13.6 GPa followed by a gradual redshift, and no significant phase transition. 86 Furthermore, the PL response in Bi perovskites is often weak and pressure-insensitive, though certain mixed-halide Bi compounds have shown slight activation under compression. 86 For instance, a sharp increase in the PL intensity until 13.4 GPa was observed in the mixed-halide Cs₃Bi₂I₆Cl₃. ⁸⁶ The 6s² lone pair of Bi³⁺ contributes to local structural distortion, but its stereochemical activity is less pronounced than in Sn²⁺ or Pb²⁺, resulting in reduced exciton

Open Access Article. Published on 28 Mphalane 2025. Downloaded on 2025-11-04 19:45:23.

localization and diminished light emission under pressure. As a result, Bi³⁺-based 2D perovskites may be more suited for applications requiring structural robustness and environmental stability rather than dynamic optoelectronic tunability. Nonetheless, ongoing efforts to enhance their emissive properties through halide alloying, organic spacer modification, and external stimuli like pressure continue to expand the design space for stable, lead-free perovskite materials.

Figure 19. Behavior of MA₃Bi₂Br₉ under high pressure. (a) ADXRD spectra upon compression, (b) UV-Vis absorption spectra upon compression, and (c) bandgap as a function of pressure. Reproduced from ref. 85 with permission from American Chemical Society, copyright 2019.

Sn²⁺-based compounds offer good compressibility and bandgap tunability but suffer from oxidation. Cu²⁺ systems offer similar properties to Sn²⁺ systems with the added bonus of reduced oxidation, but Cu-Cl systems exhibit wider bandgaps and thus a lower probability for reaching the desired SQ limit. Ge²⁺ systems are also less prone to redox instability but require pressure to activate their emissive states. Bi³⁺ perovskites are structurally robust but have limited optical responsiveness. Despite these differences, all four lead-free systems benefit from pressure-tuning as a non-invasive method to modulate properties, access metastable phases, or suppress defects. For example, pressure-cycled (DA)₂GeI₄ retained broadband emission even after decompression,⁸⁴ while stabilized Sn²⁺ systems retained narrowed bandgaps post-pressure.⁷⁵ These results underscore the importance of integrating high-pressure studies into the evaluation of next-generation lead-free perovskites. Table 3 summarizes structural, optical, and reversibility trends observed under pressure across Pb²⁺ Sn²⁺, Cu²⁺, Ge²⁺, and Bi³⁺-based 2D HOIPs.

Table 3. Comparison of pressure-induced structural and optical behavior across lead-based and lead-free 2D perovskites.

This table contrasts the high-pressure responses of Pb-based 2D HOIPs with those of Sn, Cu, Ge, and Bi analogues. Pb-based systems exhibit rich polymorphism and strong bandgap tunability but raise toxicity concerns. Sn-based systems display even greater bandgap shifts and compressibility, though they suffer from oxidation instability. Cu-based systems (especially Cu-Br) combine tunability with greater environmental stability, whereas Cu-Cl analogues have wider bandgaps and limited photovoltaic relevance. Ge-based systems are underexplored but show promising pressure-activated photoluminescence and significant bandgap narrowing. Bi-based layered perovskites are structurally robust with only mild optical responses. Taken together, these comparisons underscore the potential of pressure as a universal tool for accessing metastable phases and tailoring properties in both lead and lead-free 2D HOIPs.

6. Perspective and Outlook: Pressure as a Materials Design Tool

6.1. Conclusions

High-pressure research has opened a genuinely new control axis for 2D hybrid perovskites (2D HOIPs). Unlike chemical substitution, pressure enables continuous and reversible tuning of interlayer spacing, bond angles, and orbital overlap, thereby reshaping band structures and excitonic landscapes at will. In both Ruddlesden–Popper (RP) and Dion–Jacobson (DJ) phases, compression drives a spectrum of structural responses—from subtle order–disorder rearrangements to sequential polymorphic transitions and, at higher loads, amorphization—each with distinct optoelectronic signatures. This direct structure–property leverage has already yielded robust demonstrations of bandgap modulation (red/blue shifts), exciton conversion (FE↔STE), photoluminescence (PL) enhancement, and even rare elastic responses such as negative linear compressibility (NLC) in soft-spacer systems, together with metastable-state retention upon decompression that preserves desirable properties for device-relevant conditions.

A central, unifying insight is the role of spacer chemistry. Soft, van-der-Waals-separated RP systems (e.g., BA, CMA) accommodate layer sliding/tilting and often show gradual, reversible tuning with pressure, while rigid, H-bond-connected DJ frameworks favor more abrupt or isostructural transitions and can quench PL when distortion pathways dominate. This RP-DJ contrast maps cleanly onto optical behavior—RP materials frequently show pressure-enhanced PL or reversible emission shifts; DJ analogues more often exhibit spectral abruptness and quenching—providing practical design rules for pressure-tolerant emitters and detectors.

Beyond acting as a diagnostic probe, pressure also serves as a synthetic handle. Several RP systems (e.g., PEA/Br, MHy/Br, triazolium/Br) demonstrate pressure-activated broadband emission via self-trapped excitons; lead-free analogues such as (DA)₂GeI₄ and tin-based RP families show strong bandgap tunability and, in some cases, post-pressure retention of narrowed gaps or broadband PL. These case studies illustrate the potential of compression to discover and then "lock in" hidden phases and emissive states that are difficult to access under ambient conditions through chemistry alone.

Finally, the lead-free landscape is converging with the pressure toolbox. Sn²⁺ systems offer large tunability but face oxidation; Cu²⁺ (especially Cu–Br) combines stability with promising gaps; Ge²⁺ remains underexplored yet exhibits pressure-activated emission; Bi³⁺ frameworks are robust but optically conservative. Taken together, these advances establish pressure as a universal, non-invasive route to compare, tune, and stabilize both Pb- and Pb-free chemistries toward environmentally responsible optoelectronics. Collectively, they underscore the emerging role of pressure as a true materials-design parameter for 2D HOIPs—one that complements composition and dimensionality to expand the accessible property space for adaptive photonics, sensing, and energy devices.

6.2. Outlook

Building on these advances, several directions can guide the next stage of progress:

• Quantitative structure–property maps under true hydrostatic conditions

Many reported anomalies (e.g., blueshift→redshift crossovers, non-monotonic trends) hinge on subtle balances between octahedral tilting and bond contraction, which are sensitive to pressure media and gradients. A priority is standardized hydrostatic protocols (medium choice, loading, calibration) paired with parameterized descriptors (Pb–X–Pb angles, axial/equatorial bond compressibilities) to enable cross-study comparability and predictive design.

• Correlative, time-resolved in-situ measurements

Linking phase transitions to optical responses demands synchronized ADXRD/Raman/FTIR with PL/UV-vis in the same DAC and at identical pressure points. Adding TRPL will quantify trap suppression vs STE formation kinetics; combined with variable-temperature and decompression cycles, this will separate reversible tuning from metastable trapping with device relevance.

• Metastable-state engineering ("pressure-quench" pathways)

Several systems retain narrower bandgaps or enhanced PL after pressure release, suggesting pathways to strain-lock useful states. Systematic maps of load-hold-release protocols (rates, dwell times, partial unloads) could turn pressure into a post-synthetic step akin to annealing—particularly attractive for broadband emitters and near-ideal bandgaps in lead-free families. Additionally, pressure-induced compaction of interlayer spacing could offer practical stability benefits by limiting diffusion pathways for moisture ingress — a concept supported by studies on

DJ-phase perovskites, where tighter interlayer connectivity is known to enhance humidity resistance. This suggests that pressure tuning may not only unlock new optical states but also passively improve environmental durability.

Spacer-directed mechanics: designing softness vs rigidity

The RP-DJ divide is a design lever. Soft spacers (e.g., aliphatic, cyclic) favor large, smooth tunability (and phenomena like NLC), while rigid, bifunctional spacers (DJ) enforce connectivity that can stabilize or sharply redirect transitions. Rational spacer engineering—including π -rigid, H-bonding, or ionic crosslinks—should target predictable compressibility and desired PL pathways (FE vs STE).

• Lead-free platforms with pressure-assisted stabilization

A particularly urgent frontier is the stabilization of Pb-free perovskites under pressure. For Snbased systems, combining hydrostatic compression with tight redox control and mapping retention windows could turn transient narrowing into usable states. Pressure can also serve as a rapid screening tool, linking compressibility descriptors with tunability and persistence to identify promising compositions. Beyond Sn, Cu-Br compounds and emerging Ag-Bi/Sb layered analogues deserve exploration as intrinsically more stable and environmentally benign candidates, with pressure guiding their optimization and eventual integration into devices.

Theory/simulation/ML: closing the experiment–theory loop

First-principles calculations should be used to deconvolute angle vs bond-length contributions to band dispersion under pressure. Building open datasets that connect pressure, structure, and optical properties for representative RP/DJ chemistries will enable machine learning models to predict critical pressures, phase sequences, STE onsets, and retention windows. Tight closed-loop workflows—where theory guides experimental pressure ranges and experiments iteratively refine models—will accelerate discovery and deliver prescriptive design rules for pressure-responsive, lead-free 2D perovskites.

Author Contributions

This article is licensed under a Creative Commons Attribution-NonCommercial 3.0 Unported Licence

Open Access Article. Published on 28 Mphalane 2025. Downloaded on 2025-11-04 19:45:23.

Aditya Kutty: Methodology, formal analysis, investigation, writing – original draft, review & editing, Yang Song: Conceptualization, methodology, formal analysis, investigation, writing – review & editing, supervision, funding acquisition.

Open Access Article. Published on 28 Mphalane 2025. Downloaded on 2025-11-04 19:45:23

Conflict of Interest

There are no conflicts of interest to declare

Acknowledgments

This work was supported by a Discovery Grant (RGPIN-2020-06422), and an Alliance International Catalyst Quantum Grant (ALLRP- 580885-2022) from the Natural Science and Engineering Research Council of Canada.

References

- (1) A. K. Jena, A. Kulkarni, T. Miyasaka, Chem. Rev., 2019, 119, 3036-3103.
- (2) P. Roy, A. Ghosh, F. Barclay, A. Khare, E. Cuce, *Coatings*, 2022, 12, 1089.
- (3) R. Sharif, A. Khalid, S. W. Ahmad, A. Rehman, H. G. Qutab, H. H. Akhtar, K. Mahmood, S. Afzal, F. A. Saleem, *Nanoscale Adv.*, 2023, **5**, 3803-3833.
- (4) R. A. Afre, D. Pugliese, *Micromachines*, 2024, **15**, 192.
- (5) B. Saparov, D. B. Mitzi, Chem. Rev., 2016, 116, 4558-4596.
- (6) L. Mao, C. C. Stoumpos, M. G. Kanatzidis, J. Am. Chem. Soc., 2019, 141, 1171-1190.
- (7) W. Fu, C. Pan, A. Zhou, P. Shi, Z. Yi, Q. Zeng, *Materials*, 2024, 17, 6284.
- (8) S. Li, Y. Jiang, J. Xu, D. Wang, Z. Ding, T. Zhu, B. Chen, Y. Yang, M. Wei, R. Guo, Y. Hou, Y. Chen, C. Sun, K. Wei, S. M. H. Qaid, H. Lu, H. Tan, D. Di, J. Chen, M. Grätzel, E. H. Sargent, M. Yuan, *Nature*, 2024, 635, 82-88.
- (9) J. Guo, B. Wang, D. Lu, T. Wang, T. Liu, R. Wang, X. Dong, T. Zhou, N. Zheng, Q. Fu, Q, Z. Xie, X. Wan, G. Xing, Y. Chen, Y. Liu, *Adv. Mater*, 2023, **35**, 2212126.
- (10) M. Zhang, C. Wu, M. Yin, H. Yao, H. Qiu, J. Luo, J. Du, F. Hao, *Adv. Funct. Mater.*, 2024, **34**, 2410772.
- (11) N. P. Jasti, I. Levine, Y. Feldman, G. Hodes, S. Aharon, D. Cahen, *PNAS*, 2024, **121**, e2316867121.
- (12) C. C. Stoumpos, M. G. Kanatzidis, Acc. Chem. Res., 2015, 48, 2791-2802.
- (13) C. Ortiz-Cervantes, P. Carmona-Monroy, D. Solis-Ibarra, *ChemSusChem*, 2019, **12**, 1560-1575.
- (14) E. R. Dohner, A. Jaffe, L. R. Bradshaw, H. I. Karunadasa, *J. Am. Chem. Soc.*, 2014, **136**, 13154-13157.

- (15) H. Tsai, W. Nie, J.-C. Blancon, C. C. Stoumpos, R. Asadpour, B. Harutyunyan, A. J. Neukirch, R. Verduzco, J. J. Crochet, S. Tretiak, L. Pedesseau, J. Even, M. A. Alam, G. Gupta, J. Lou, P. M. Ajayan, M. J. Bedzyk, M. G. Kanatzidis, A. D. Mohite, *Nature*, 2016, **536**, 312-316.
- (16) J. Hu, L. Yan, W. You, Adv. Mater., 2018, **30**, 1802041.
- (17) A. Burgos-Caminal, E. Socie, M. E. F. Bouduban, J.-E. Moser, *J. Phys. Chem. Lett.*, 2020, **11**, 7692-7701.
- (18) L. Mao, W. Ke, L. Pedesseau, Y. Wu, C. Katan, J. Even, M. R. Wasielewski, C. C. Stoumpos, M. G. Kanatzidis, *J. Am. Chem. Soc.*, 2018, **140**, 3775-3783.
- (19) S. Liu, S. Sun, C. K. Gan, A. G. del Águila, Y. Fang, J. Xing, T. T. H. Do, T. J. White, H. Li, W. Huang, Q. Xiong, *Sci. Adv.*, 2019, **5**, eaav9445.
- (20) Y. Qin, Z. Lv, S. Chen, W. Li, X. Wu, L. Ye, N. Li, P. Lu, J. Phys. Chem. C, 2019, 123, 22491-22498.
- (21) T. Yin, B. Liu, J. Yan, Y. Fang, M. Chen, W. K. Chong, S. Jiang, J.-L. Kuo, J. Fang, P. Liang, S. Wei, K. P. Loh, T. C. Sum, T. J. White, Z. X. Shen, *J. Am. Chem. Soc.*, 2019, **141**, 1235-1241.
- (22) Y. Yuan, X.-F. Liu, X. Ma, X. Wang, X. Li, J. Xiao, X. Li, H.-L. Zhang, L. Wang, *Adv. Sci.*, 2019, **6**, 1900240.
- (23) Y. Fang, L. Zhang, Y. Yu, X. Yang, K. Wang, B. Zou, CCS Chem., 2020, 3, 2203-2210.
- (24) V. Gómez, S. Klyatskaya, O. Fuhr, S. Kalytchuk, R. Zbořil, M. Kappes, S. Lebedkin, M. Ruben, *Inorg. Chem.*, 2020, **59**, 12431-12436.
- (25) L. Kong, G. Liu, J. Gong, L. Mao, M. Chen, Q. Hu, X. Lü, W. Yang, M. G. Kanatzidis, H.-k. Mao, *PNAS*, 2020, **117**, 16121-16126.
- (26) H. Li, Y. Qin, B. Shan, Y. Shen, F. Ersan, E. Soignard, C. Ataca, S. Tongay, *Adv. Mater.*, 2020, **32**, 1907364.
- (27) X. Ren, X. Yan, D. V. Gennep, H. Cheng, L. Wang, Y. Li, Y. Zhao, S. Wang, *Appl. Phys. Lett.*, 2020, **116**, 101901.
- (28) P. Shen, T. Vogt, Y. Lee, J. Phys. Chem. Lett., 2020, 11, 4131-4137.
- (29) C. Tian, Y. Liang, W. Chen, Y. Huang, X. Huang, F. Tian, X. Yang, *Phys. Chem. Chem. Phys.*, 2020, **22**, 1841-1846.
- (30) R. Fu, W. Zhao, L. Wang, Z. Ma, G. Xiao, B. Zou, *Angew. Chem. Int. Ed.*, 2021, **60**, 10082-10088.
- (31) F. F. Gao, X. Li, Y. Qin, Z.-G. Li, T.-M. Guo, Z.-Z. Zhang, G.-D. Su, C. Jiang, M. Azeem, W. Li, X. Wu, X.-H. Bu, *Adv. Opt. Mater.*, 2021, **9**, 210003.
- (32) H. Li, D. Wines, B. Chen, K. Yumigeta, Y. M. Sayyad, J. Kopaszek, S. Yang, C. Ataca, E. H. Sargent, S. Tongay, *ACS Appl. Mater. Interfaces*, 2021, **13**, 44964-44971.
- (33) L. A. Muscarella, A. Dučinskas, M. Dankl, M. Andrzejewski, N. P. M. Casati, U. Rothlisberger, J. Maier, M. Graetzel, B. Ehrler, J. V. Milić, *Adv. Mater.*, 2022, **34**, 2108720.

Article. Published on 28 Mphalane 2025. Downloaded on 2025-11-04 19:45:23

- (35) F.-F. Gao, H. Song, Z.-G. Li, Y. Qin, X. Li, Z.-Q. Yao, J.-H. Fan, X. Wu, W. Li, X.-H. Bu, *Angew. Chem. Int. Ed.*, 2023, **62**, e202218675.
- (36) J. Ratté, M. F. Macintosh, L. DiLoreto, J. Liu, W. Mihalyi-Koch, M. P. Hautzinger, I. A. Guzei, Z. Dong, S. Jin, Y. Song, *J. Phys. Chem. Lett.*, 2023, **14**, 403-412.
- (37) T. Yin, H. Yan, I. Abdelwahab, Y. Lekina, X. Lü, W. Yang, H. Sun, K. Leng, Y. Cai, Z. X. Shen, K. P. Loh, *Nat. Commun.*, 2023, **14**, 411.
- (38) F.-F. Gao, Y. Qin, Z.-G. Li, W. Li, J. Hao, X. Li, Y. Liu, C. J. Howard, X. Wu, X. Jiang, Z. Lin, P. Lu, X.-H. Bu, *ACS Nano*, 2024, **18**, 3251-3259.
- (39) S. Guo, W. Mihalyi-Koch, Y. Mao, X. Li, K. Bu, H. Hong, M. P. Hautzinger, H. Luo, D. Wang, J. Gu, Y. Zhang, D. Zhang, Q. Hu, Y. Ding, W. Yang, Y. Fu, S. Jin, X. Lü, *Nat. Commun.*, 2024, **15**, 3001.
- (40) M. Mączka, J. A. S. Silva, W. P. Gomes, D. L. M. Vasconcelos, F. Dybała, A. P. Herman, R. Kudrawiec, P. T. C. Freire, *J. Phys. Chem. C*, 2024, **128**, 8698-8707.
- (41) S. Sobczak, A. Nowok, J. K. Zaręba, K. Roszak, A. Półrolniczak, A. Z. Szeremeta, B. Dziuk, F. Dybała, S. Pawlus, R. Kudrawiec, A. Sieradzki, M. Mączka, A. Katrusiak, *J. Mater. Chem. A*, 2024, **12**, 16803-16814.
- (42) P. Steeger, M. Adnan, T. Deilmann, X. Li, S. Müller, K. Skrzyńska, M. Hanfland, E. Kolesnikov, J. Kösters, T. Block, R. Schmidt, I. Kupenko, C. Sanchez-Valle, G. V. Prakash, S. M. de Vasconcellos, R. Bratschitsch, *J. Am. Chem. Soc.*, 2024, **146**, 23205-23211.
- (43) M. Szafrański, J. Mater. Chem. A, 2024, 12, 2391-2399.
- (44) H. Zhang, P. Zhang, C. Xie, J. Han, B. Xu, Z. Quan, Adv. Sci., 2024, 11, 2305597.
- (45) A. Kutty, J. Ratté, R. Guan, J. Liu, S. Tao, Y. Lin, M. P. Hautzinger, W. Mihalyi-Koch, S. Jin, Y. Song, *Adv. Opt. Mater.*, 2025, 2500602.
- (46) Y. Yin, X. Yan, H. Luo, Y. Liang, P. Xu, Y. Wang, S. Jin, W. Tian, *Angew. Chem. Int. Ed.*, 2025, **64**, e202418587.
- (47) G. Liu, J. Gong, L. Kong, R. D. Schaller, Q. Hu, Z. Liu, S. Yan, W. Yang, C. C. Stoumpos, M. G. Kanatzidis, H.-k. Mao, T. Xu, *PNAS*, 2018, **115**, 8076-8081.
- (48) Y. Moritomo, Y. Tokura, J. Chem. Phys., 1994, 101, 1763-1766.
- (49) A. Jaffe, Y. Lin, H. I. Karunadasa, ACS Energy Lett., 2017, 2, 1549-1555.
- (50) Y. Chen, R. Fu, L. Wang, Z. Ma, G. Xiao, K. Wang, B. Zou, *J. Mater. Chem. A*, 2019, **7**, 6357-6362.
- (51) C. Gao, R. Li, Y. Li, R. Wang, M. Wang, Z. Gan, L. Bai, Y. Liu, K. Zhao, S. F. Liu, Y. Cheng, W. Huang, *J. Phys. Chem. Lett.*, 2019, **10**, 5687-5693.
- (52) L. Zhang, L. Wu, K. Wang, B. Zou, Adv. Sci., 2019, 6, 1801628.

- (53) S. Guo, Y. Zhao, K. Bu, Y. Fu, H. Luo, M. Chen, M. P. Hautzinger, Y. Wang, S. Jin, W. Yang, X. Lü, *Angew. Chem. Int. Ed.*, 2020, **59**, 17533-17539.
- (54) G. Xiang, Y. Wu, M. Zhang, C. Cheng, J. Leng, H. Ma, Nanomaterials, 2021, 11, 2712.
- (55) M. Mączka, S. Sobczak, P. Ratajczyk, F. F. Leite, W. Paraguassu, F. Dybała, A. P. Herman, R. Kudrawiec, A. Katrusiak, *Chem. Mater.*, 2022, **34**, 7867-7877.
- (56) M. Mączka, F. Dybała, A. P. Herman, W. Paraguassu, A. J. Barros dos Santos, R. Kudrawiec, *RSC Adv.*, 2024, **14**, 38514-38522.
- (57) S. Attique, N. Ali, T. Imran, S. Rauf, A. Khesro, S. Ali, W. Wang, R. Khatoon, A. Abbas, E. Ullah khan, S. Yang, H. Wu, *Sol. Energy*, 2022, **239**, 198-220.
- (58) A. Celeste, F. Capitani, J. Appl. Phys., 2022, 132, 220903.
- (59) N. Wang, S. Zhang, S. Wang, X. Yang, F. Guo, Y. Zhang, Z. Gu, Y. Song, *Adv. Funct. Mater.*, 2024, **34**, 2315918.
- (60) A. Jayaraman, Rev. Mod. Phys., 1983, 55, 65-108.
- (61) W. A. Bassett, High Press. Res., 2009, 29, 163-186.
- (62) S. Klotz, J. C. Chervin, P. Munsch, G. Le Marchand, J. Phys. D: Appl. Phys., 2009, 42, 075413.
- (63) D. Zhaohui, Y. Song, in *Nanowires Fundamental Research*, ed. H. Abbass, IntechOpen, 2011, Ch. 23, 527-552.
- (64) Z. Dong, PhD thesis, University of Western Ontario, 2012.
- (65) Z. Dong, Y. Song, J. Phys. Chem. C, 2010, 114, 1782-1788.
- (66) J. Ratté, MSc thesis, University of Western Ontario, 2022.
- (67) Y. Xu, T. Gong, J. N. Munday, Sci. Rep., 2015, 5, 13536.
- (68) K. Wang, L. Zheng, Y. Hou, A. Nozariasbmarz, B. Poudel, J. Yoon, T. Ye, D. Yang, A. V. Pogrebnyakov, V. Gopalan, S. Priya, *Joule*, 2022, 6, 756-771.
- (69) M. Pitaro, E. K. Tekelenburg, S. Shao, M. A. Loi, *Adv. Mater.*, 2022, **34**, 2105844.
- (70) A. Filippetti, S. Kahmann, C. Caddeo, A. Mattoni, M. Saba, A. Bosin, M. A. Loi, *J. Mater. Chem. A*, 2021, **9**, 11812-11826.
- (71) C. C. Stoumpos, C. D. Malliakas, M. G. Kanatzidis, *Inorg. Chem.*, 2013, **52**, 9019-9038.
- (72) H.-H. Fang, S. Adjokatse, S. Shao, J. Even, M. A. Loi, *Nat. Commun.*, 2018, 9, 243.
- (73) M. Morana, L. Malavasi, Sol. RRL, 2021, 5, 2100550.
- (74) M. Konstantakou, T. Stergiopoulos, J. Mater. Chem. A, 2017, 5, 11518-11549.
- (75) L. Kong, J. Gong, I. Spanopoulos, S. Yan, Z. Li, Z. Zhu, X. Liu, Y. Zhu, H. Dong, H. Shu, Q. Hu, W. Yang, H.-k. Mao, M. G. Kanatzidis, G. Liu, *Adv. Funct. Mater.*, 2024, **34**, 2414437.

Article. Published on 28 Mphalane 2025. Downloaded on 2025-11-04 19:45:23

- (77) J. Wen, K. Rong, L. Jiang, C. Wen, B. Wu, B. Sa, Y. Qiu, R. Ahuja, *Nano Energy*, 2024, **128**, 109802.
- (78) S. Dutta, S. K. D. Vishnu, S. Som, R. Chaurasiya, D. K. Patel, K. Moovendaran, C.-C. Lin, C.-W. Chen, R. Sankar, *ACS Appl. Electron. Mater.*, 2022, 4, 521-530.
- (79) X. Zhan, X. Jiang, P. Lv, J. Xu, F. Li, Z. Chen, X. Liu, *Angew. Chem. Int. Ed.*, 2022, **61**, e202205491.
- (80) A. Jaffe, S. A. Mack, Y. Lin, W. L. Mao, J. B. Neaton, H. I. Karunadasa, *Angew. Chem. Int. Ed.*, 2020, **59**, 4017-4022.
- (81) Q. Li, S. Li, K. Wang, Z. Quan, Y. Meng, B. Zou, J. Phys. Chem. Lett., 2017, 8, 500-506.
- (82) Y. Zhou, D. Zhao, F. Wang, Y. Shi, Z. Ma, R. Fu, K. Wang, Y. Sui, Q. Dong, G. Xiao, B. Zou, *Phys. Rev. Mater.*, 2023, **7**, 074002.
- (83) R. Chiara, M. Morana, L. Malavasi, *ChemPlusChem*, 2021, **86**, 879-888.
- (84) M. Morana, R. Chiara, B. Joseph, T. B. Shiell, T. A. Strobel, M. Coduri, G. Accorsi, A. Tuissi, A. Simbula, F. Pitzalis, A. Mura, G. Bongiovanni, L. Malavasi, *iScience*, 2022, **25**, 104057.
- (85) Q. Li, L. Yin, Z. Chen, K. Deng, S. Luo, B. Zou, Z. Wang, J. Tang, Z. Quan, *Inorg. Chem.*, 2019, **58**, 1621-1626.
- (86) J. Zhang, M. Li, D. Wang, B. Chu, S. Zhang, Q. Xu, K. Wang, *J. Mater. Chem. A*, 2023, **11**, 19427-19434.

Table 1. Pressure-induced phase transitions or structural modifications in 2D hybrid perovskites.

Perovskite	Type	Spacer Type	Phase Transitions / Structural Modifications	Critical Pressure (GPa)	Ref
(PEA) ₂ PbI ₄	RP	Rigid	AB → AA stacking	5.8	[51]
(BA) ₂ PbI ₄	RP	Soft	Isostructural ($Pbca I \rightarrow Pbca II$) \rightarrow amorphous	~ 0.5, ~ 4.77	[20]
			$Pbca (1b \rightarrow 1a) \rightarrow P2_1/a \rightarrow amorphous$	$0.1, \sim 1.6, \sim 5.2$	[21]
			$Pbca \rightarrow Pbca \rightarrow \text{uncorrugated phase} \rightarrow P2_1/a$	0.17, 2, 3	[22]
(BA) ₂ PbBr ₄	RP	Soft	I (PbBr ₆ octahedra and BA tilting)	~ 3.7	[26]
· /-			$Pbca \rightarrow P2_1/c$	0.3	[28]
(BA) ₂ (MA)Pb ₂ Br ₇	RP	Soft	I (PbBr ₆ octahedra tilting, BA and MA rotation)	3.4-4.8	[26]
			II (PbBr ₆ octahedra tilting, BA and MA rotation)	4.8-8.1	
(OA) ₂ PbI ₄	RP	Soft	$LP (Pbca) \rightarrow (LP + HP (Pbca + P2_1/a) \rightarrow HP (P2_1/a) \rightarrow$	~ 0.5, ~ 2.17, ~ 7.29	[20]
			amorphous		
(DDA) ₂ PbI ₄	RP	Soft	$LP (Pbca) \rightarrow LP + HP (Pbca + P2_1/a) \rightarrow HP (P2_1/a) \rightarrow$	~ 0.8, ~ 4.09, ~ 10.17	[20]
			amorphous		
(PMA) ₂ PbI ₄	RP	Rigid	$Pbca \rightarrow Pccn \rightarrow isostructural$	4.6, 7.7	[29]
$(GA)_2PbI_4$	RP	Soft	Isostructural	5.5	[32]
$(BzA)_2PbBr_4$	RP	Rigid	Isostructural	0.15-0.25	[33]
$(CMA)_2PbI_4$	RP	Soft	Isostructural phase transition and NLC → amorphous	~ 1.1–1.3	[36]
MHy ₂ PbI ₄	RP	Soft	Phase II $(Pmcn) \rightarrow Phase V (Pmmn) \rightarrow Phase VI (Pmn2_1) \rightarrow$	0.22, 1.15, 3.00	[41]
-			Phase VII $(P2_1)$		
MHy ₂ PbBr ₄	RP	Soft	Phase III $(Pmn2_1) \rightarrow Phase IV (P2_1) \rightarrow Phase V (P2_12_12_1)$	~ 4, ~ 4.4	[43]
			Phase III $(Pmn2_1) \rightarrow Phase IV (P2_1)$	~ 4	[55]
(Tz) ₂ PbBr ₄	RP	Rigid	Phase I \rightarrow Phase III \rightarrow Phase IV	2.4, 6, 8–8.5	[56]
(2meptH ₂)PbCl ₄	DJ	Rigid	Isostructural (unit cell volume collapse)	2.1	[34]
IMMHyPbBr ₄	DJ	Rigid	First order (abrupt shifts of Raman modes)	~ 1.25–1.53	[40]
(API)PbBr ₄	DJ	Rigid	Isostructural (abrupt unit cell volume change)	2.7	[46]
DPDAPbI ₄	DJ	Rigid	Isostructural (unusual octahedral distortion) → amorphous	~ 0–2	[45]

Journal of Materials Chemistry A

Table 2. Summary of high-pressure effects on optoelectronic properties of 2D hybrid perovskites.

14 19:45:23	្លើ Be 35 of 58 Journal of Materials Chemistry A											
Open Access Article. Published on 28 M (cc) BY-NC This article is Licensed und	Table 2. Summary of high-pressure effects on optoelectronic properties of 2D hybrid perovskites.											
	2D Perovskite	2D Perovskite Pressure Range of Range (GPa) PL Enhancement (GPa)		Bandgap Modulation Range (eV)	Pressure Effects on Optical Properties ^a	Reversibility ^b	Ref					
	(PEA) ₂ PbI ₄ 0–8 N/A N/A		12	N/A direct–indirect transition at 5.8 GPa	PL: RS with CI → DI → quenching PL: RS with DI of peak 1 (2.16 eV) → quenching; AE: RS → abrupt BS	PR (PL) PR (PL, BG)	[19] [51]					
	(PEA) ₂ PbBr ₄	0–48	N/A	$2.99 \rightarrow 2.35$	PL: RS with DI→ quenching; AE: RS → abrupt BS → re-RS; BG: BR → BW → BR	PR (PL) IR (BG)	[27]					
		0–30	4.0–8.0 (STE)	$2.96 \rightarrow 2.46$	PL (FE): RS with DI → quenching; PL (STE at ~ 4 GPa) EI → DI → quenching; AE: RS → abrupt BS → re-RS; BG: BR → BW → BR	R (PL, BG)	[52]					
	PEA) ₂ PbCl ₄	0–30	0–0.4 (STE) 2.1–4.6 (FE)	$3.57 \rightarrow 3.13$	PL (STE): BS → RS; PL (FE): RS; PL (STE & FE): EI (5-fold) → DI → quenching; AE: RS → quenching; BG: significant BR	IR (PL, BG)	[30]					
	(BA) ₂ PbI ₄	0–11	0.85–1.07; 3.09–8.7	N/A	PL(FE): RS → quenching; PL2: RS with EI → DI → quenching; PL3 (~3.10 GPa): → RS with EI → quenching	PR (PL)	[20]					
		0–10	N/A	N/A	PL: all RS;	PR (PL)	[21]					
		0–40	0–2.6 (PL 1)	$2.28 \rightarrow 0.95$	AE: abrupt initial BS → RS PL1: abrupt initial BS → RS with EI → quenching; PL2: (at 2.6 GPa) → DI → quenching; PL3: (at 9.2 GPa) → quenching; AE: abrupt BS → RS; BG: BW → BR	R (BG) IR (PL, BG)	[22]					
	$(BA)_2(MA)Pb_2I_7$	0–10	N/A	N/A	PL1 &2: RS \rightarrow peaks merge \rightarrow BS \rightarrow quenching	R (PL)	[37]					

0 12	NT/A	2.5 1.0	DI TAE DE DE : :C + DD	D (DI DC)	[26]	
	**		, ,	/		
0-20	\ /	$\sim 3.0 \rightarrow 2.55$		R (PL, BG)	[28]	
	3.4–12.9 (STE)					H
			AE: RS \rightarrow BS; BG: BR \rightarrow BW			
0–15	N/A	$\sim 2.25 \rightarrow 1.9$	PL: RS \rightarrow BS with DI \rightarrow quenching;	R (PL, BG)	[26]	S
			AE: RS \rightarrow BS; BG: BR \rightarrow BW			
0–13	1.48-4.70 (PL2)	N/A	PL1 (FE): RS with DI \rightarrow quenching;	PR (PL)	[20]	
			$PL2 (\sim 1.48 \text{ GPa}) \rightarrow EI \rightarrow \text{quenching}$			
0–14	0.41-2.12 (PL3)	N/A	$PL1(FE)$: RS with DI \rightarrow quenching;	PR (PL)	[20]	Ī
	· · ·		PL2 (at 0.41 GPa): RS with DI→ quenching;	, ,		0
			PL3 (at 0.41 GPa): RS with EI \rightarrow DI \rightarrow quenching;			5
			PL4 (at 1.79 GPa): RS → quenching			0
0-10	0–1.5	$2.24 \to 1.85$, , ,	PR (PL)	[23]	2
			1 67			A
0–2	N/A	N/A	PL: moderate RS with DI	PR (PL)	[24]	A
0-20	N/A	$2.19 \to 1.26$	RS of absorption edge \rightarrow slight BS \rightarrow re-RS;	/		
			1 0 0			
0–15	N/A	$2.55 \to 2.33$	PL: RS \rightarrow BS \rightarrow quenching;	N/A	[32]	- 53
			AE: RS \rightarrow BS; BG: BR \rightarrow BW			
0-0.35	N/A	$2.36 \rightarrow 2.327$	PL: RS; AE: RS; BG: BR	R (PL, BG)	[33]	1
0-0.35	N/A	$3.07 \rightarrow 3.015$	PL: RS; AE: RS; BG: BR	R (PL, BG)	[33]	Q
0–7	N/A	N/A	PL: RS with CI	R (PL)	[35]	S
0–8	N/A	N/A	PL: RS with CI	R (PL)	[35]	<u>a</u>
0–15	0-0.8	$2.33 \to 1.89$	PL(FE): RS with 10-fold EI \rightarrow DI \rightarrow quenching;	R (PL, BG)	[36]	B
			AE: RS; BG: significant BR			at
0–18	0-0.6 (STE)	N/A	PL (STE): BS with EI \rightarrow DI \rightarrow quenching;	R (PL)	[38]	Ž
	0.6–2.59 (FE)		PL(FE at 0.60 GPa): RS with EI \rightarrow DI \rightarrow quenching			+
0–7	~ 0–1.75	$2.03 \to 1.86$	$PL(FE)$: RS with EI \rightarrow quenching;	R (PL, BG)	[41]	7
			AE: RS; BG: substantial BR			Ø
0–8	N/A	~ 2.4 → 2.0	PL: RS \rightarrow BS with DI	R (PL, BG)	[42]	
			AE: RS \rightarrow BS; significant BR \rightarrow BW			
0–7	N/A	$2.90 \to 2.723$	AE: RS; BG: BR → BW	R (BG)	[43]	7
0–8	0.07-4.49	$2.812 \rightarrow 2.662$	PL (FE): RS \rightarrow BS with 11-fold EI \rightarrow quenching;	/		
			AE: RS \rightarrow BS; BG: BR \rightarrow BW		'	
	0-13 0-14 0-10 0-2 0-20 0-15 0-0.35 0-0.35 0-7 0-8 0-15 0-18 0-7 0-8 0-7	0-20 0-0.9 (FE) 3.4-12.9 (STE) 0-15 N/A 0-13 1.48-4.70 (PL2) 0-14 0.41-2.12 (PL3) 0-10 0-1.5 0-2 N/A 0-20 N/A 0-15 N/A 0-0.35 N/A 0-0.35 N/A 0-7 N/A 0-8 N/A 0-15 0-0.6 (STE) 0.6-2.59 (FE) 0-7 N/A 0-8 N/A 0-7 N/A 0-8 N/A 0-7 N/A	0-20 0-0.9 (FE) 3.4 -12.9 (STE) $\sim 3.0 \rightarrow 2.55$ ~ 3.4 -12.9 (STE) $\sim 2.25 \rightarrow 1.9$ $\sim 2.25 \rightarrow 1.9$ ~ 0 -13 ~ 0 -14 ~ 0 -15 ~ 0 -16 ~ 0 -17 ~ 0 -18 ~ 0 -18 ~ 0 -18 ~ 0 -19	0-20 0-0.9 (FE) 3.4-12.9 (STE) ~ 3.0 → 2.55 PL: RS with EI → broad-band emission at 3.4 GPa → coexistence of blue and broad-band emission; AE: RS→BS; BG: BR → BW 0-15 N/A ~ 2.25 → 1.9 PL: RS→BS with DI → quenching; AE: RS → BS; BG: BR → BW 0-13 1.48-4.70 (PL2) N/A PL1 (FE): RS with DI → quenching; PL2 (-1.48 GPa) → EI → quenching; PL3 (at 0.41 GPa): RS with DI → quenching; PL3 (at 0.41 GPa): RS with DI → quenching; PL3 (at 0.41 GPa): RS with DI → quenching; PL4 (at 1.79 GPa): RS → 4-fold EI → DI → quenching; AE: RS; BG: significant BR 0-10 0-1.5 2.24 → 1.85 PL (FE): RS with DI → quenching; AE: RS; BG: significant BR 0-2 N/A N/A PL: moderate RS with DI 0-20 N/A 2.19 → 1.26 RS of absorption edge → slight BS → re-RS; BG: significant BR → slight BW → BR 0-15 N/A 2.55 → 2.33 PL: RS→ BS; BG: BR → BW 0-0.35 N/A 2.36 → 2.327 PL: RS; AE: RS; BG: BR 0-7 N/A N/A PL: RS; with CI 0-8 N/A N/A PL: RS with CI 0-15 0-0.8 2.33 → 1.89 PL: RS with CI 0-17 N/A N/A PL: RS with CI 0-7<	0-20 0-0.9 (FE) 3.4-12.9 (STE) ~ 3.0 → 2.55 PL: RS with EI → broad-band emission at 3.4 GPa → coexistence of blue and broad-band emission; AE: RS→BS; BG: BR → BW R (PL, BG) 0-15 N/A ~ 2.25 → 1.9 PL: RS→BS; BG: BR → BW R (PL, BG) 0-13 1.48-4.70 (PL2) N/A PL1 (FE): RS with DI → quenching; PL2 (e1.48 GPa) → EI → quenching PR (PL) 0-14 0.41-2.12 (PL3) N/A PL1(FE): RS with DI → quenching; PL2 (at 0.41 GPa): RS with DI → quenching; PL3 (at 0.41 GPa): RS with DI → quenching; PL4 (at 1.79 GPa): RS → quenching PR (PL) 0-10 0-1.5 2.24 → 1.85 PL (FE): RS → 4-fold EI → DI → quenching; PL4 (at 1.79 GPa): RS → quenching; PL5 (BC) PR (PL) 0-2 N/A N/A PL: RS, BG: significant BR PR (PL) 0-2 N/A N/A PL: RS → BS → quenching; PL (RS → BS) → Quenching; PL (RS → BS) PR (PL) 0-2.5 N/A 2.35 → 2.33 PL: RS → BS → Quenching; PL (RS → BS) N/A 0-15 N/A 2.36 → 2.327 PL: RS, AE: RS; BG: BR R (PL, BG) 0-3.5 N/A 3.07 → 3.015 PL: RS, AE: RS; BG: BR R (PL, BG) 0-8 N/A <td< td=""><td>0-20 0-0.9 (FE) 3.4-12.9 (STE) ~ 3.0 → 2.55 PL: RS with EI → broad-band emission at 3.4 GPa → coexistence of blue and broad-band emission; AE: RS→BS; BG: BR → BW R (PL, BG) [28] 0-15 N/A ~ 2.25 → 1.9 PL: RS→BS; BG: BR → BW R (PL, BG) [26] 0-13 1.48-4.70 (PL.2) N/A PL: RS→BS; with DI → quenching; PL2 (-1.48 GPa) → EI → quenching; PL2 (at 0.41 GPa): RS with DI → quenching; PL3 (at 0.41 GPa): RS with DI → quenching; PL3 (at 0.41 GPa): RS with EI → DI → quenching; PL4 (at 1.79 GPa): RS → quenching PR (PL) [20] 0-10 0-1.5 2.24 → 1.85 PL (FE): RS with DI → quenching; PL4 (at 1.79 GPa): RS → quenching PR (PL) [23] 0-2 N/A N/A PL: (FE): RS → 4-fold EI → DI → quenching; PL (FE): RS with DI PR (PL) [24] 0-20 N/A N/A PL: moderate RS with DI PR (PL) [24] 0-20 N/A 2.19 → 1.26 RS of absorption edge → slight BS → re-RS; BG: significant BR R (BG) [29] 0-15 N/A 2.55 → 2.33 PL: RS→ BS → quenching; AE: RS→ BS; BG: BR N/A [32] 0-0.35 N/A 2.36 → 2.327 PL: RS; AE: RS; BG: BR R (PL, BG)</td></td<>	0-20 0-0.9 (FE) 3.4-12.9 (STE) ~ 3.0 → 2.55 PL: RS with EI → broad-band emission at 3.4 GPa → coexistence of blue and broad-band emission; AE: RS→BS; BG: BR → BW R (PL, BG) [28] 0-15 N/A ~ 2.25 → 1.9 PL: RS→BS; BG: BR → BW R (PL, BG) [26] 0-13 1.48-4.70 (PL.2) N/A PL: RS→BS; with DI → quenching; PL2 (-1.48 GPa) → EI → quenching; PL2 (at 0.41 GPa): RS with DI → quenching; PL3 (at 0.41 GPa): RS with DI → quenching; PL3 (at 0.41 GPa): RS with EI → DI → quenching; PL4 (at 1.79 GPa): RS → quenching PR (PL) [20] 0-10 0-1.5 2.24 → 1.85 PL (FE): RS with DI → quenching; PL4 (at 1.79 GPa): RS → quenching PR (PL) [23] 0-2 N/A N/A PL: (FE): RS → 4-fold EI → DI → quenching; PL (FE): RS with DI PR (PL) [24] 0-20 N/A N/A PL: moderate RS with DI PR (PL) [24] 0-20 N/A 2.19 → 1.26 RS of absorption edge → slight BS → re-RS; BG: significant BR R (BG) [29] 0-15 N/A 2.55 → 2.33 PL: RS→ BS → quenching; AE: RS→ BS; BG: BR N/A [32] 0-0.35 N/A 2.36 → 2.327 PL: RS; AE: RS; BG: BR R (PL, BG)

	4.6
	_
	10

e 37 of 58		Journal of Materials Chemistry A				
Example 27 of 58 The control of the	0–17	0–3.5	$2.775 \rightarrow 2.25$	PL (FE): RS with EI → DI → quenching; AE: RS → slight BS → re-RS; BG: BR → slight BW → BR	IR (PL, BG)	[44]
	0–18	0–3.3 (FE) 6–8.3 (Broadband)	3.375 → 3.0	PL(STE): BS \rightarrow quenching; PL(FE): RS with EI \rightarrow DI \rightarrow quenching; AE: RS \rightarrow BS \rightarrow re-RS; BG: BR \rightarrow BW \rightarrow BR	IR (PL, BG)	[44]
Tz ₂ PbBr ₄	0–13	0–7.77	N/A	PL (FE and STE at 4.42 GPa): RS with EI \rightarrow BS with DI \rightarrow quenching	N/A	[56]
(3AMP)PbI ₄	0–30	0–6	2.10 → 1.63	PL: large RS with EI \rightarrow DI; AE: RS \rightarrow BS \rightarrow re-RS; BG: BR \rightarrow BW \rightarrow BR	IR (PL, BG)	[25]
(3AMP)(MA)Pb ₂ I ₇	0-30	N/A	$1.85 \rightarrow 1.6$	AE: RS \rightarrow BS \rightarrow re-RS; BG: BR \rightarrow BW \rightarrow BR	IR (BG)	[25]
S-[4APEA]PbI ₄	0–12	N/A	N/A	PL: RS with DI → quenching	PR (PL)	[31]
(PDMA)PbI ₄	0-0.35	N/A	$2.41 \rightarrow 2.383$	PL and AE: RS; BG: BR	R (PL, BG)	[33]
PDMA)PbBr ₄	0-0.35	N/A	$3.06 \rightarrow 3.029$	PL and AE: RS; BG: BR	R (PL, BG)	[33]
2meptH ₂)PbCl ₄	0–30	1.5–9.9	$3.55 \rightarrow 3.32$	PL: BS with 8-fold EI \rightarrow RS and DI \rightarrow quenching; AE: RS \rightarrow BS \rightarrow RS; BG: BR \rightarrow BW \rightarrow BR	N/A	[34]
MMHyPbBr ₄	0–10	~ 0–2	N/A	PL (FE): RS with EI \rightarrow DI	R (PL)	[40]
API)PbBr ₄	0–6	0–2.7	~ 3.1 → 2.75	PL(STE): BS with DI → quenching; PL (new FE): BS with EI →DI; AE: RS; BG: significant BR	R (BG)	[46]
DPDAPbI ₄	0–9	0–1.49	$2.26 \to 1.87$	PL (FE): RS with EI → DI → quenching; AE: RS; BG: significant BR	R (PL, BG)	[45]
$(GA)(MA)_2Pb_2I_7$	0–25	0–1.3	2.00 → 1.52	PL: RS with 5-fold EI → quenching; AE: RS→BS→RS; BG: BR → BW → BR	IR (PL, BG)	[50]
$(HA)_2(GA)Pb_2I_7$	0–9	0–1.59	~ 2.14 → 1.8	PL (FE): RS with 12-fold EI \rightarrow DI \rightarrow quenching; AE: RS \rightarrow BS \rightarrow RS; BG: BR \rightarrow BW \rightarrow BR	R (PL) IR (BG)	[53]
$(BA)_2(GA)Pb_2I_7$	0–5	0–2.1	2.21 → 1.91	PL(FE): RS with 72-fold EI → DI; AE: RS → quenching; BG: BR	N/A	[39]

^a RS = Redshift; BS = Blueshift;

CI = Constant intensity; DI = Decreasing intensity; EI = Enhancing intensity

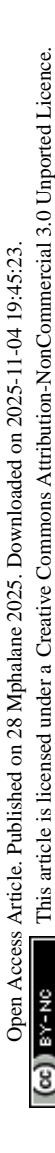
FE= Free exciton; STE = Self-trapped exciton

^b R = Reversible; IR = Irreversible; PR = Partially reversible

Table 3. Comparison of high-pressure behavior between lead-based and lead-free 2D perovskites.^a

8	Journ	al of Materials Chemistry A	
Table 3. Comparis Property Bandgap Photoluminescence	son of high-pressure behavior between le	ead-based and lead-free 2D perovskites. ^a	
Property	Lead-Based (Pb ²⁺) Lead-Free (Sn ²⁺ , Cu ²⁺ , Ge ²⁺ , Bi ³⁺)	Representative Examples [Refs]	
Bandgap	 Redshift and bandgap reduction Redshift → blueshift 	1. ETA ₂ PbI ₄ [23], (Bz) ₂ PbI ₄ [33], (Bz) ₂ PbBr ₄ [33], (PDMA)PbBr ₄ [33], (CMA) ₂ PbI ₄ [36], DPDAPbI ₄ [45]	
	2. Redsnift → bluesnift 3. Initial blueshift → redshift	2. (BA) ₂ (MA)Pb ₂ Br ₇ [26], (GA) ₂ PbI ₄ [32], MHy ₂ PbBr ₄ [43,55] 3. (BA) ₂ PbI ₄ [22]	
	4. Initial redshift → abrupt	3. (BA) ₂ PO ₁₄ [22] 4. (3AMP)PbI ₄ [25], (3AMP)(MA)Pb ₂ I ₇ [25], (PEA) ₂ PbBr ₄ [27,52],	
	blueshift → re-redshift	(PMA) ₂ PbI ₄ [29], (GA)(MA) ₂ Pb ₂ I ₇ [50], (HA) ₂ (GA)Pb ₂ I ₇ [53]	
	Redshift (Sn^{2+} , Cu^{2+} , Ge^{2+}); stable or weak shift (Bi^{3+})	(BA) ₂ (MA)Sn ₂ I ₇ [75], (PMA) ₂ CuBr ₄ [79], (EA) ₂ CuBr ₄ [80], DABCuCl ₄ [81], (PEA) ₂ CuCl ₄ [82], (DA) ₂ GeI ₄ [84], Cs ₃ Bi ₂ Br ₉ [54], MA ₃ Bi ₂ Br ₉ [8. Cs ₃ Bi ₂ I ₆ Cl ₃ [86]	
Photoluminescence	1. Gradual decrease → quenching	1. (PEA) ₂ PbI ₄ [19,51], (BA) ₂ (MA)Pb ₂ Br ₇ [26], S-[4APEA]PbI ₄ [31], (BA) ₂ (MA)Pb ₂ I ₇ [37]	
	2. Initial enhancement → gradual reduction → quenching	2. (BA) ₂ PbI ₄ [20,22], ETA ₂ PbI ₄ [23], (CMA) ₂ PbI ₄ [36], DPDAPbI ₄ [45]	
	STE activation in Ge^{2+} ; weak in Bi^{3+}	$(DA)_2GeI_4$ [84], $Cs_3Bi_2I_6Cl_3$ [86]	
Compressibility	High (smaller B_0)	(BA) ₂ PbI ₄ [20,21,22], (CMA) ₂ PbI ₄ [36]	
	Sn^{2+} , Ge^{2+} : comparable; Bi^{3+} : lower	$(BA)_2(MA)Sn_2I_7$ [75], $(DA)_2GeI_4$ [84], $MA_3Bi_2Br_9$ [85]	
Phase transitions	Multiple and often reversible	(PEA) ₂ PbI ₄ [19,51], (BA) ₂ PbI ₄ [20,21,22], (PMA) ₂ PbI ₄ [29], Tz ₂ PbI ₄ [5	
	Fewer in Sn^{2+} , Cu^{2+} , Ge^{2+} ; less	(BA) ₂ (MA)Sn ₂ I ₇ [75], (EA) ₂ CuBr ₄ [80], DABCuCl ₄ [81], (DA) ₂ GeI ₄ [84	
	pronounced in Bi ³⁺	$MA_3Bi_2Br_9$ [85]	
Metastability	Observed in select compositions	(GA)(MA) ₂ Pb ₂ I ₇ [50], (HA) ₂ (GA)Pb ₂ I ₇ [53]	
	In Sn^{2+} , Ge^{2+} only	$(BA)_2(MA)Sn_2I_7$ [75], $(DA)_2GeI_4$ [84]	
PL persistence post-	Common	(PEA) ₂ PbI ₄ [19,51], (CMA) ₂ PbI ₄ [36], DPDAPbI ₄ [45]	
compression	In Ge^{2+} ; rare in Bi^{3+}	$(DA)_2GeI_4$ [84]	

^a Lead-Based are in normal font and Lead-Free are in *italic*.



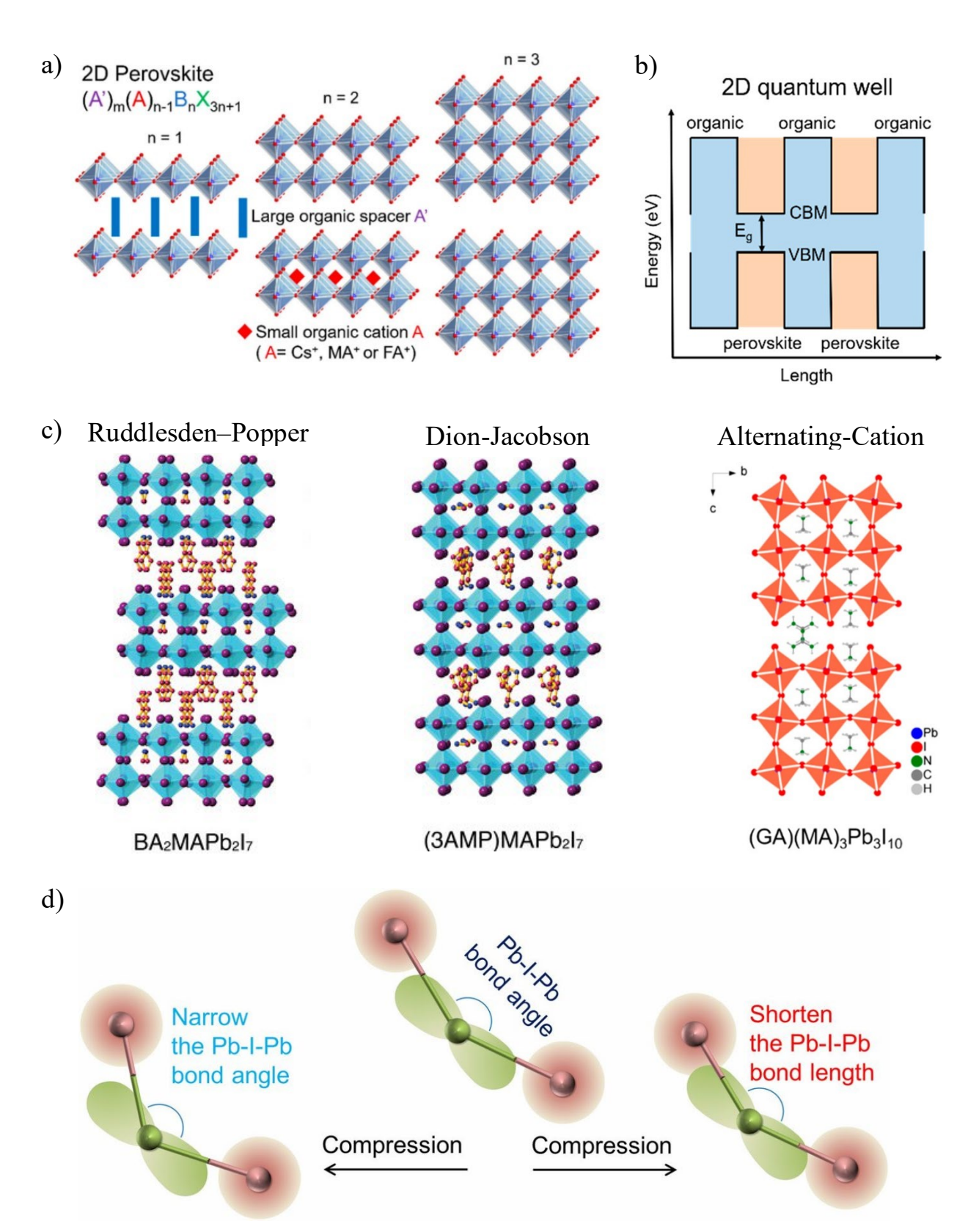


Figure 1. Structure of 2D HOIPs. (a) Crystal structure for n = 1, 2, and 3, (b) electronic structure showing 2D multiple quantum well [6], (c) RP, DJ [13], and alternating cation 2D HOIP crystal structure [6], and (d) effect of external pressure on Pb-I-Pb bond angle and Pb-I bond length [47].

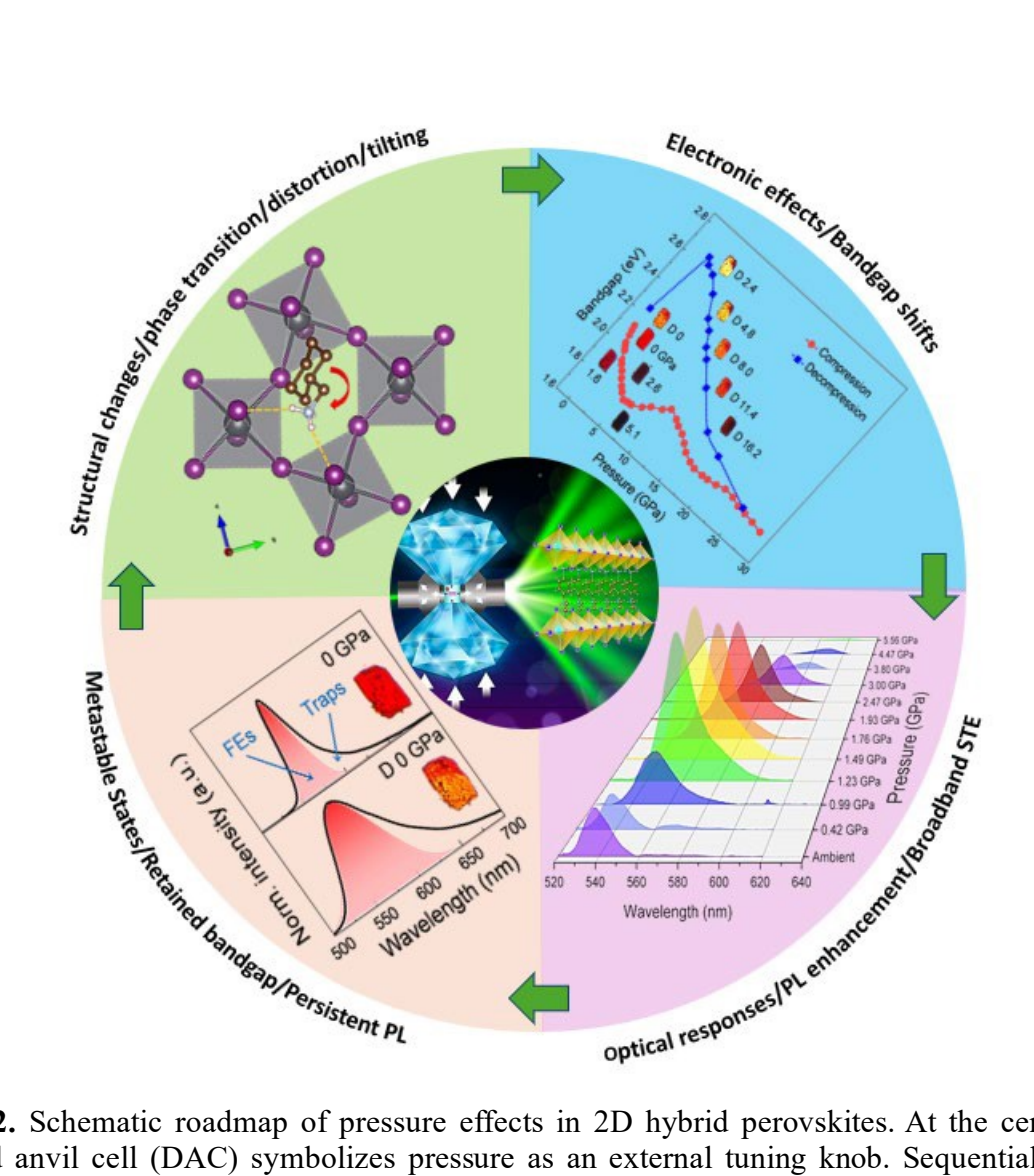


Figure 2. Schematic roadmap of pressure effects in 2D hybrid perovskites. At the center, the diamond anvil cell (DAC) symbolizes pressure as an external tuning knob. Sequential arrows highlight the cascade of responses under compression: (i) structural changes such as phase transitions, octahedral tilting, and eventual amorphization; [36] (ii) electronic effects including bandgap narrowing, anomalous widening, and direct–indirect conversions; [53] (iii) optical responses ranging from photoluminescence enhancement to broadband self-trapped exciton (STE) emission; [45] and (iv) metastable states where narrowed gaps or persistent PL remain after decompression. [53] Together, these links illustrate how pressure serves not only as a probe but also as a design pathway for uncovering and stabilizing functional states in 2D perovskites.

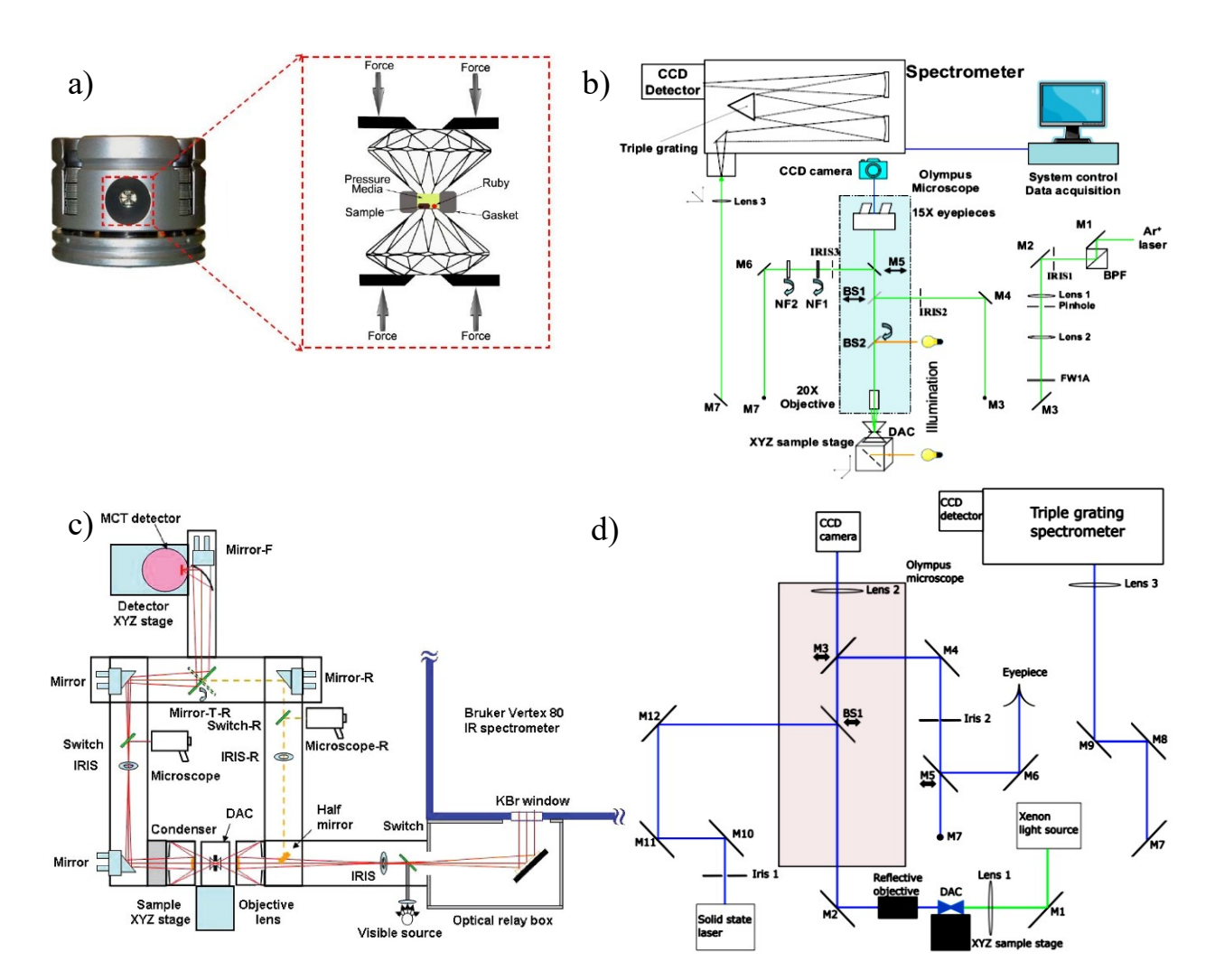


Figure 3. High-pressure setup and instrumentation. (a) Schematic of DAC [63], (b) Raman set up [64], (c) FTIR set up [65], and (d) PL, UV-vis set up [66].

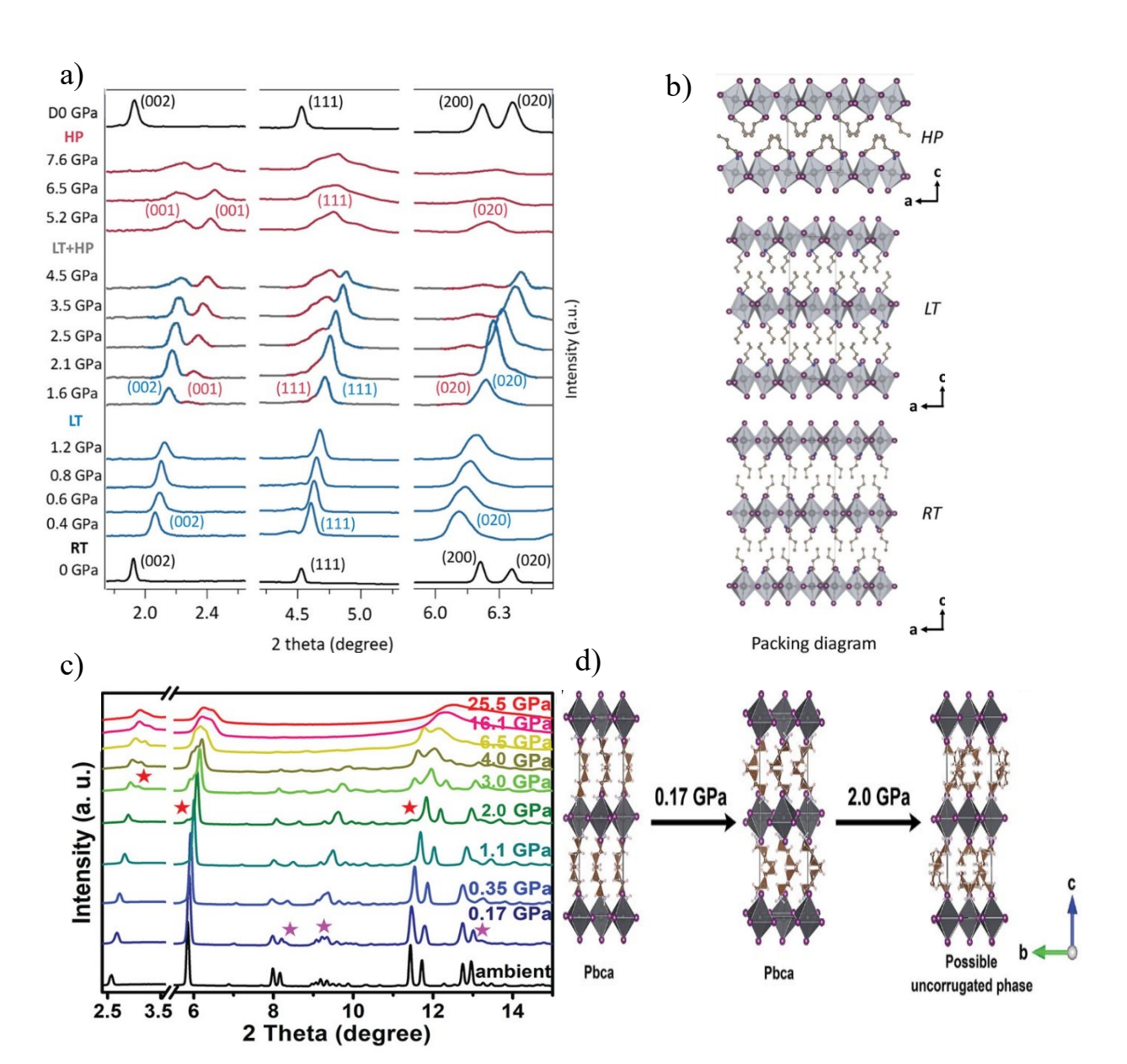


Figure 4. Sequential phase transitions of RP-type (BA)₂PbI₄. (a) In situ XRD spectra upon compression to 7.6 GPa and (b) schematic of crystal structures in the RT, LT, and HP phases [21]. (c) XRD spectra upon compression to 25.5 GPa and (d) schematic of change in crystal structure from ambient pressure to 2.0 GPa [22].

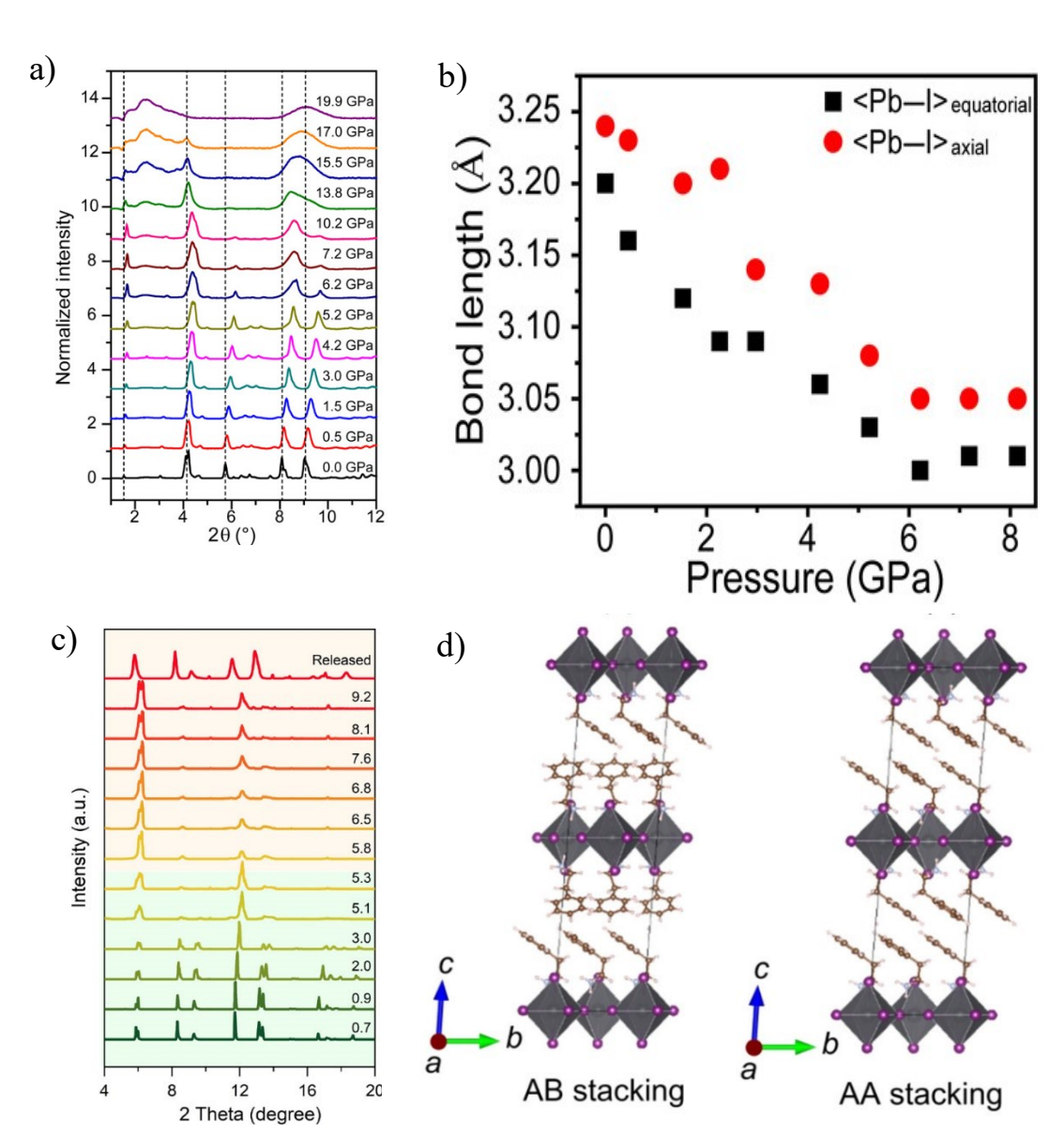


Figure 5. Subtle structural transition of RP-type (PEA)₂PbI₄. (a) XRD spectra upon compression to 19.9 GPa and (b) Pb-I bond lengths as functions of pressure [19]. (c) XRD spectra upon compression to 9.2 GPa and (d) Crystal structures showing both AB and AA stacking arrangements [51].

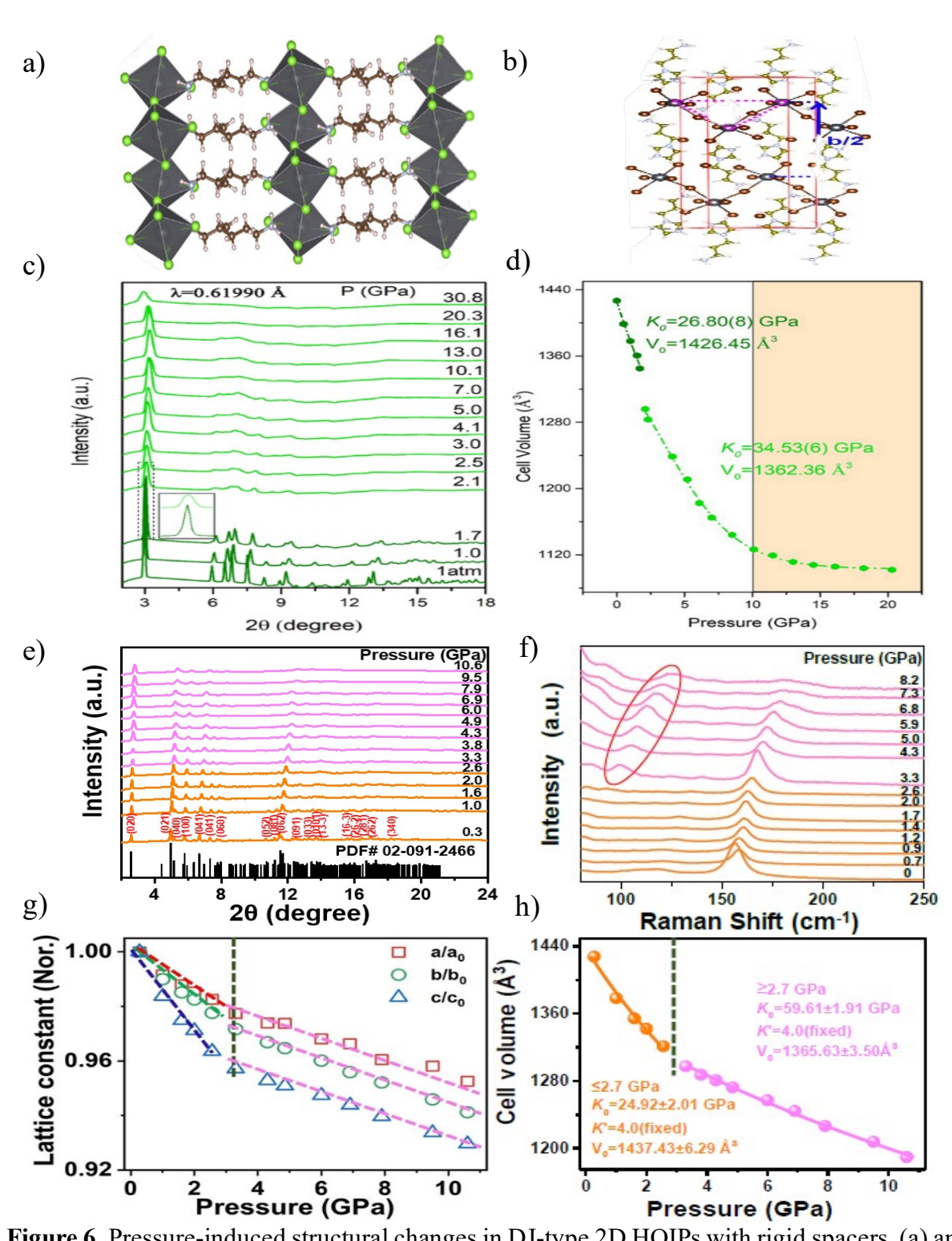


Figure 6. Pressure-induced structural changes in DJ-type 2D HOIPs with rigid spacers. (a) and (b) Crystal structures at ambient pressure of (2meptH₂)PbCl₄ and (API)PbBr₄, respectively [34,46]. (c) and (d) In situ ADXRD spectra upon compression to 30.8 GPa and unit cell volume as a function of pressure of (2meptH₂)PbCl₄ [34]. (e)–(h) In situ XRD spectra upon compression to 10.6 GPa, Raman spectra upon compression to 8.2 GPa, normalized unit cell parameters as functions of pressure, and unit cell volume as a function of pressure of (API)PbBr₄ [46].

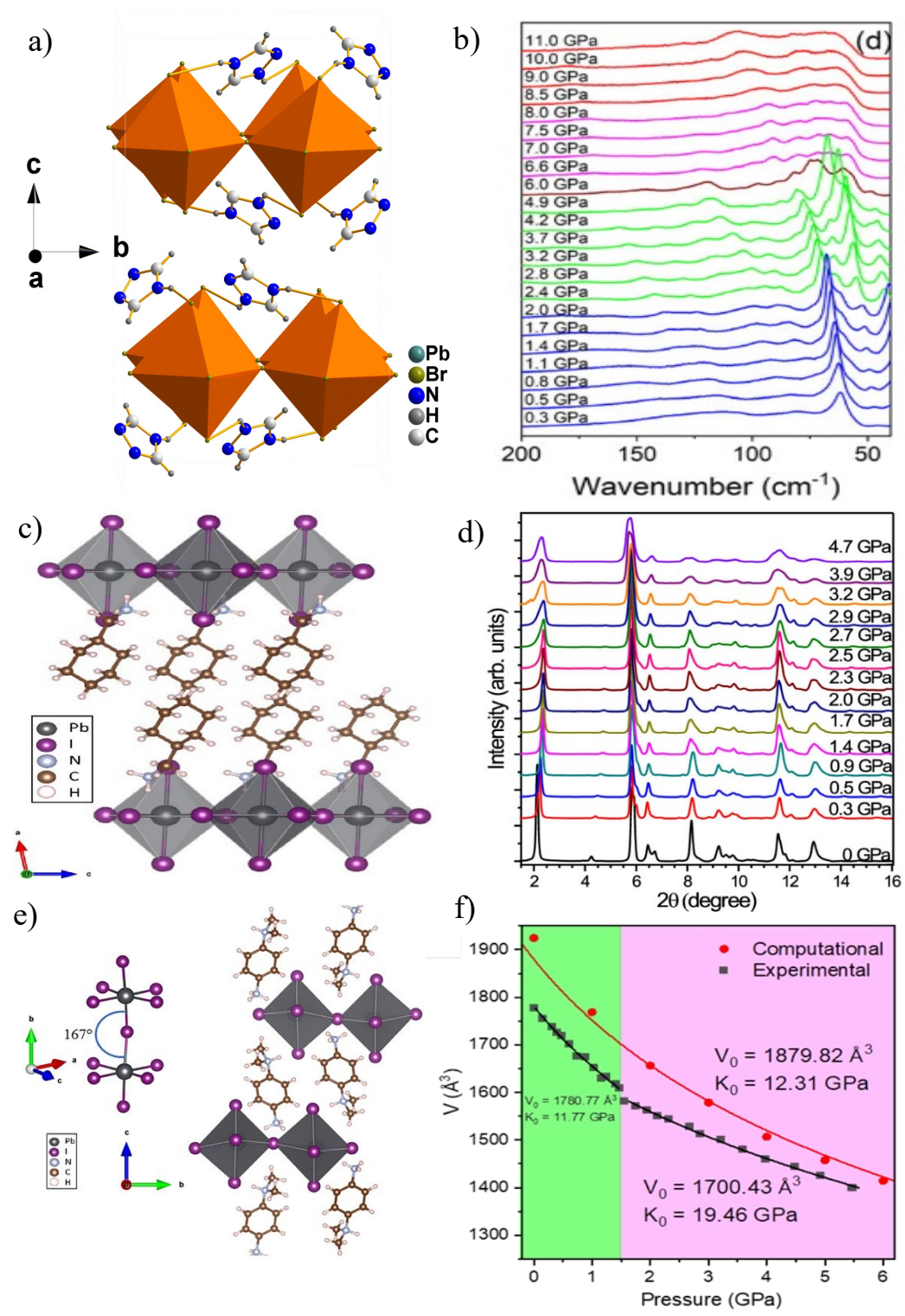


Figure 7. Space-influenced pressure-induced structural changes of 2D HOIPs. (a) Crystal structure of Tz₂PbBr₄ at ambient pressure and (b) representative Raman spectra of Tz₂PbBr₄ in the 200–40 cm⁻¹ range [56]. (c) Crystal structure of (CMA)₂PbI₄ at ambient pressure and (d) ADXRD spectra upon compression at selected pressures [36]. (e) Crystal structure of DPDAPbI₄ at ambient pressure and (f) normalized unit cell volume as a function of pressure [45].



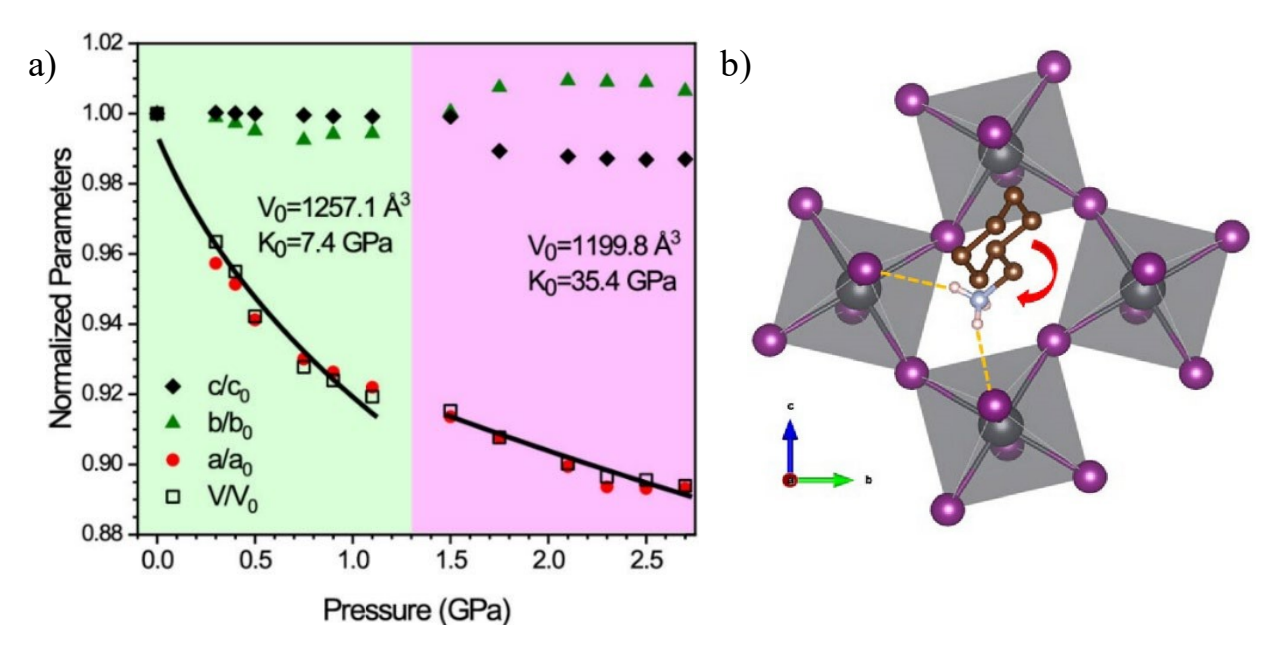


Figure 8. Pressure-induced rare phenomena in $(CMA)_2PbI_4$. (a) Normalized unit cell parameters and unit cell volume as functions of pressure showing NLC along the *b* direction and (b) possible rotation of the CMA ring (shown by red arrow) along the *a*-axis [36].

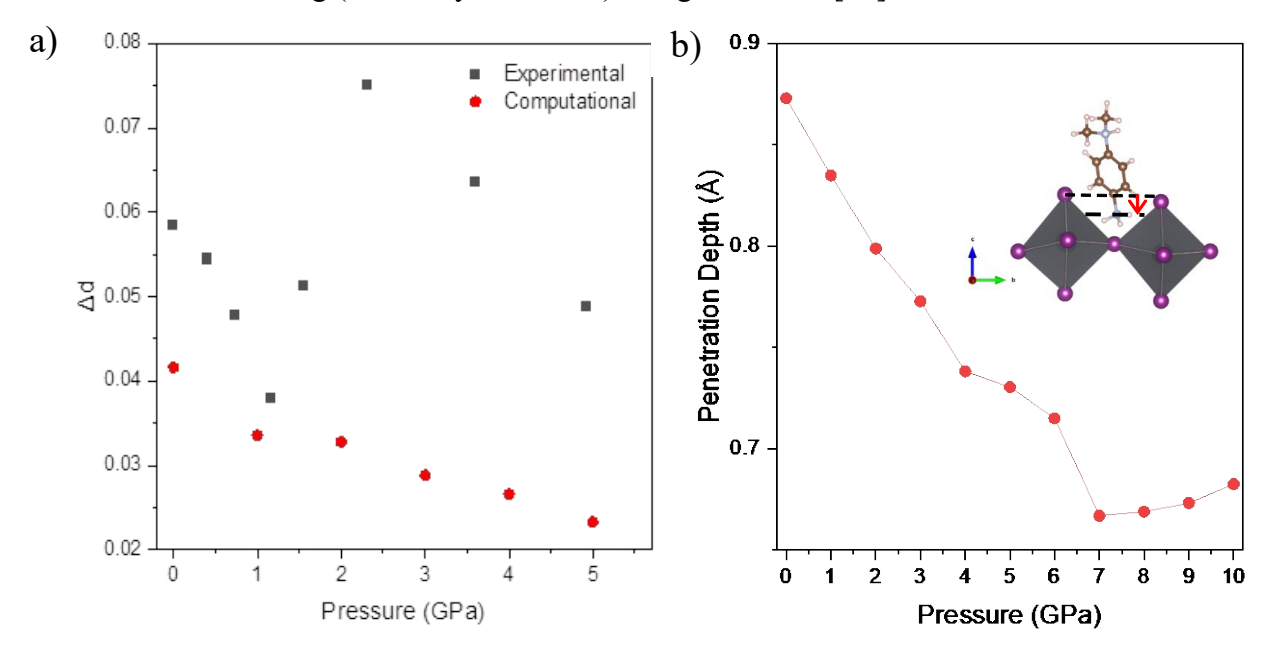


Figure 9. Pressure-induced uncommon phenomena in DPDAPbI₄. (a) bond length distortion as a function of pressure showing relaxation of octahedral distortion at low pressure and (b) penetration depth of DPDA spacer as a function of pressure [45].

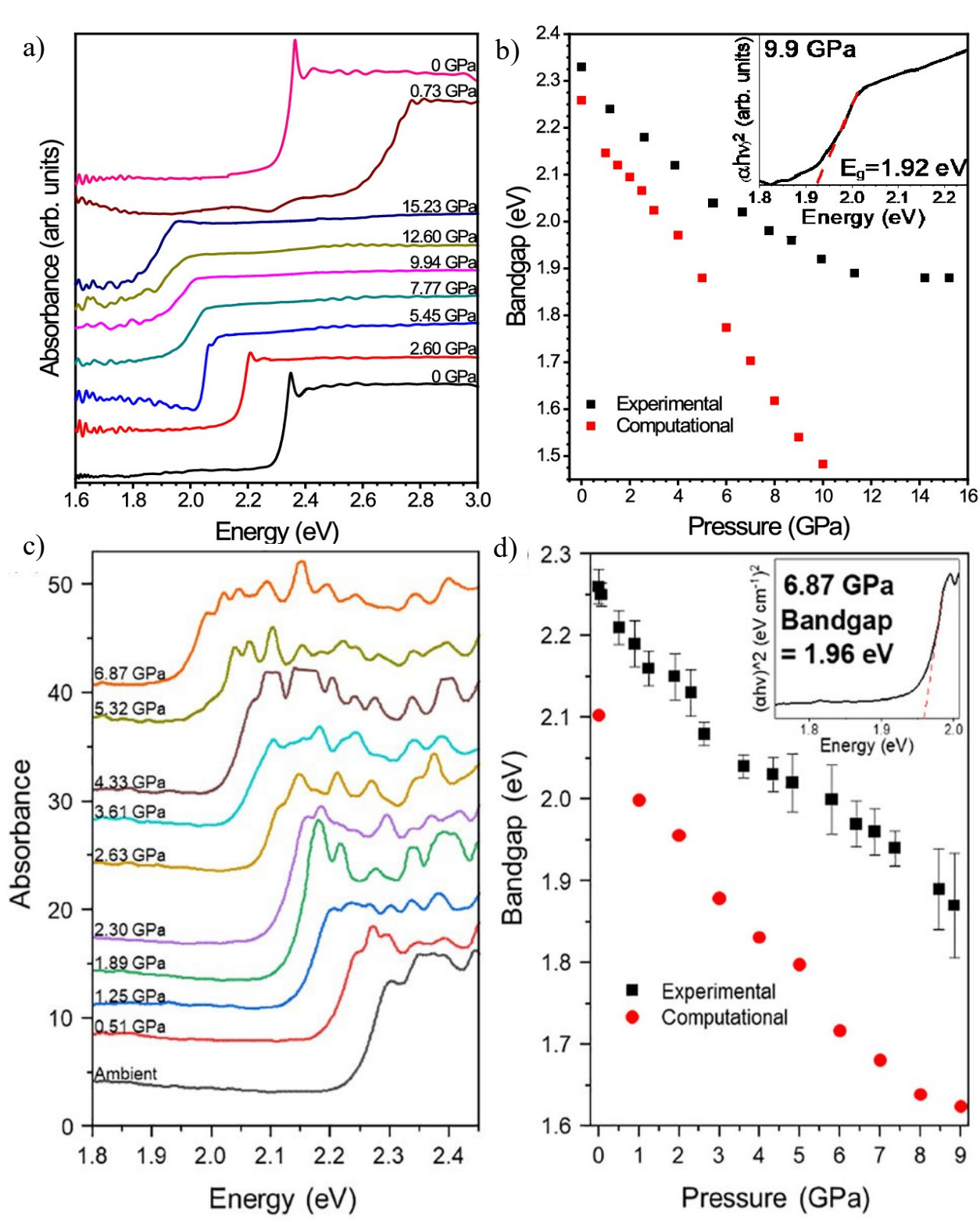
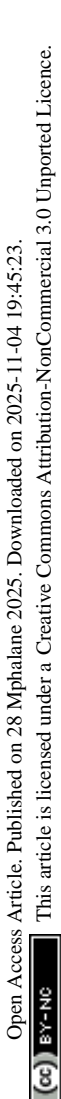


Figure 10. Pressure-induced optical absorbance behavior of 2D HOIPs with differing organic spacers. (a) In situ UV-Vis absorption spectra upon compression to 15.23 GPa and (b) bandgap as a function of pressure for (CMA)₂PbI₄ [36]. (c) In situ UV-Vis absorption spectra upon compression to 6.87 GPa and (d) bandgap as a function of pressure for DPDAPbI₄ [45].



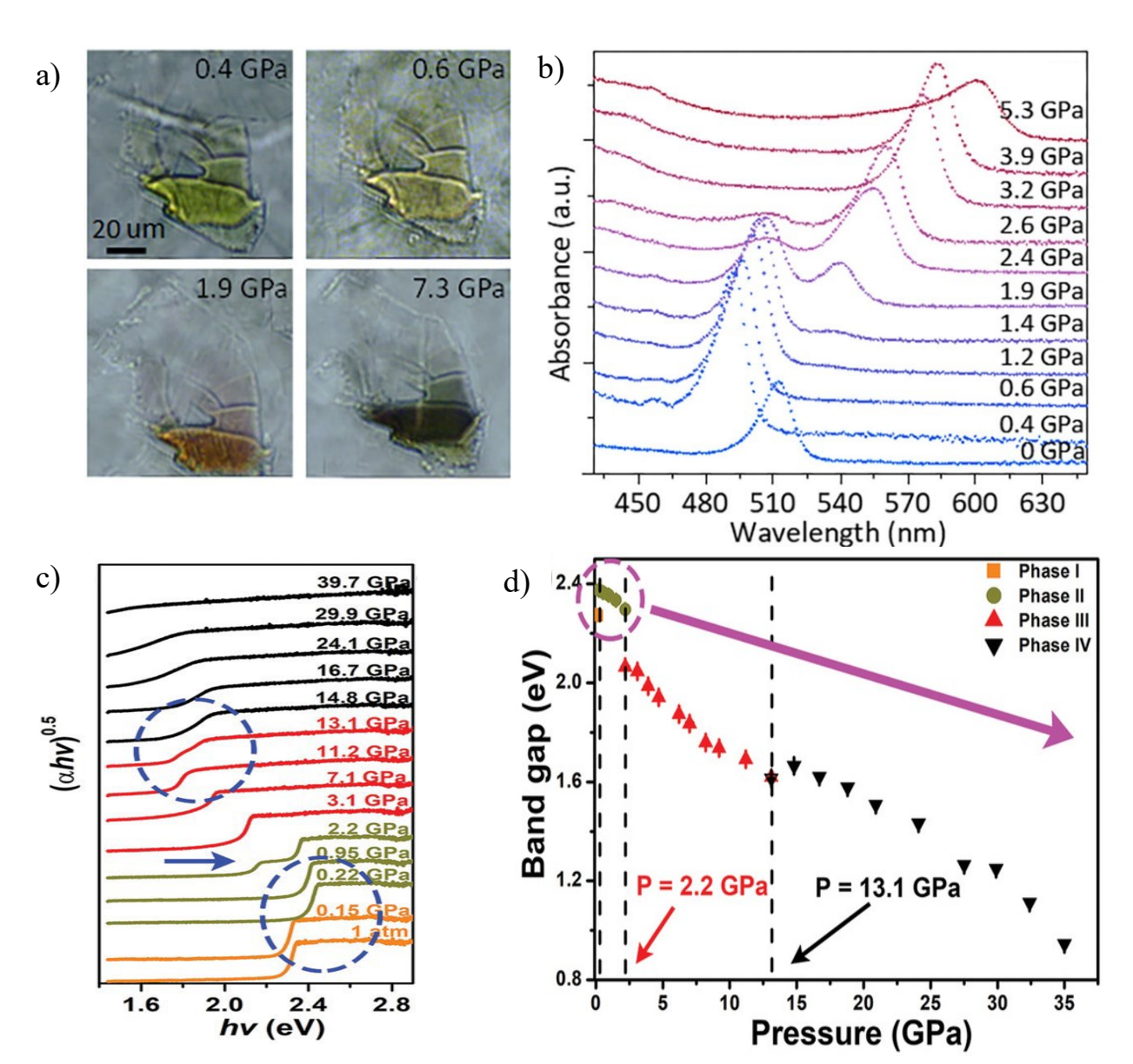


Figure 11. Pressure-induced optical absorbance behavior of (BA)₂PbI₄. (a) Optical images at selected pressures illustrating piezochromism and (b) In situ UV-Vis absorption spectra [21]. (c) In situ UV-Vis absorption spectra upon compression to 39.7 GPa and (d) bandgap as a function of pressure [22].

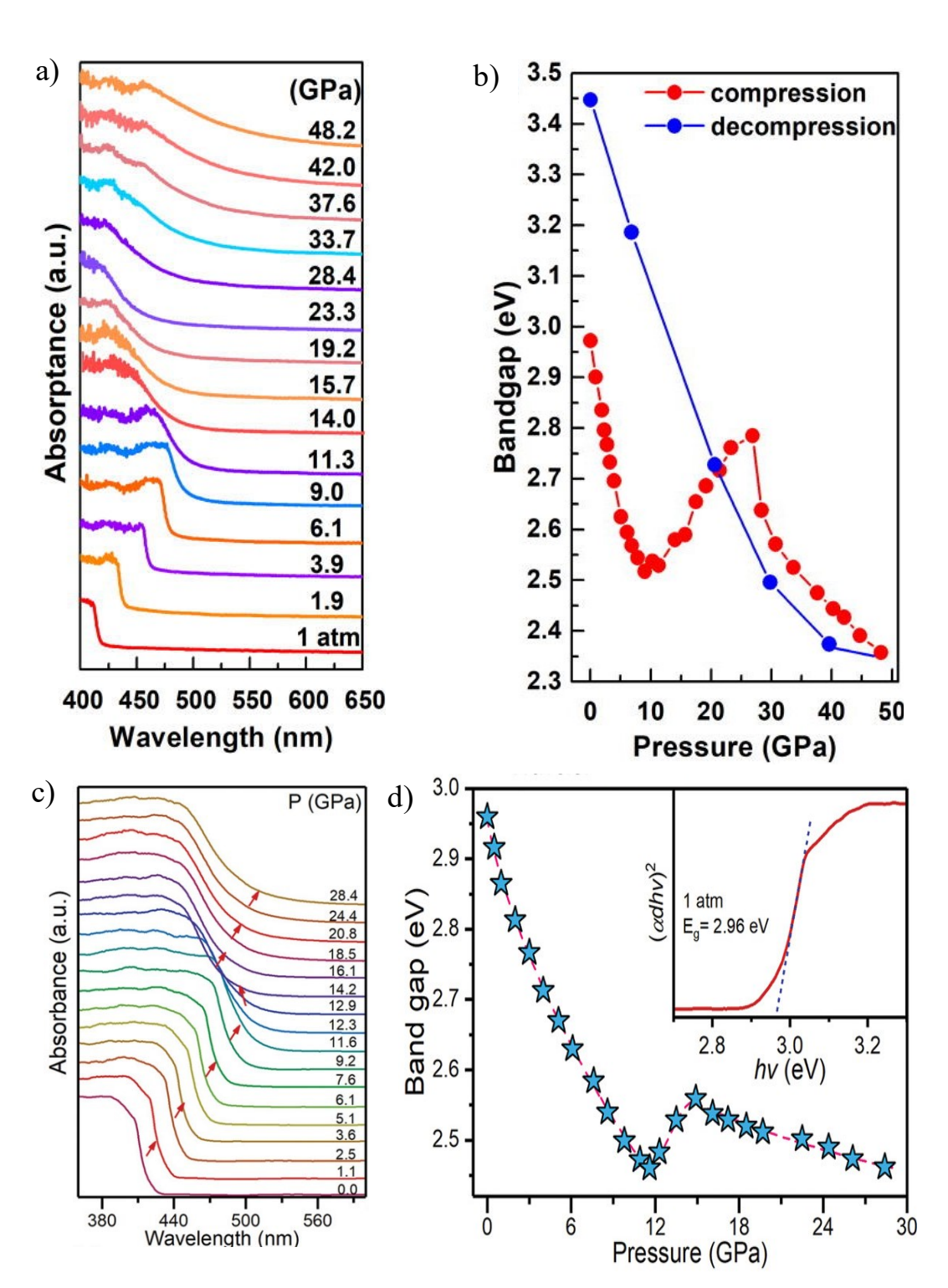


Figure 12. Pressure-induced optical absorbance behavior of (PEA)₂PbBr₄. (a) In situ UV-Vis absorption spectra upon compression to 48.2 GPa and (b) bandgap as a function of pressure [27]. (c) In situ UV-Vis absorption spectra upon compression to 28.4 GPa and (d) bandgap as a function of pressure [52].



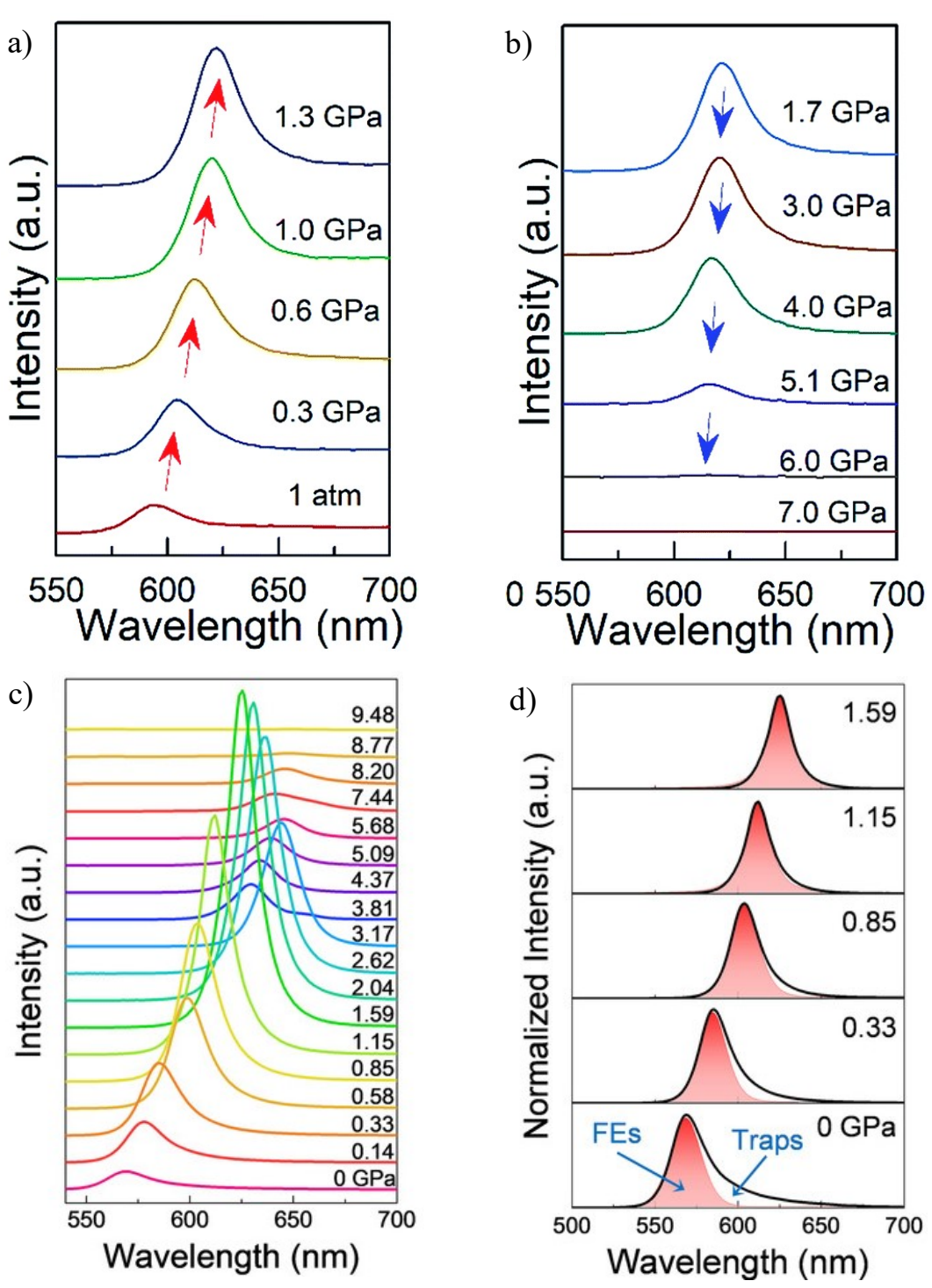


Figure 13. Pressure-induced PL enhancement of GA-based 2D HOIPs. (a) and (b) In situ PL spectra upon compression to 1.3 and 7.0 GPa respectively for (GA)(MA)₂Pb₂I₇ [50]. (c) and (d) In situ PL spectra upon compression to 9.48 GPa and fitted PL spectra at selected pressures for (HA)₂(GA)Pb₂I₇ [53].

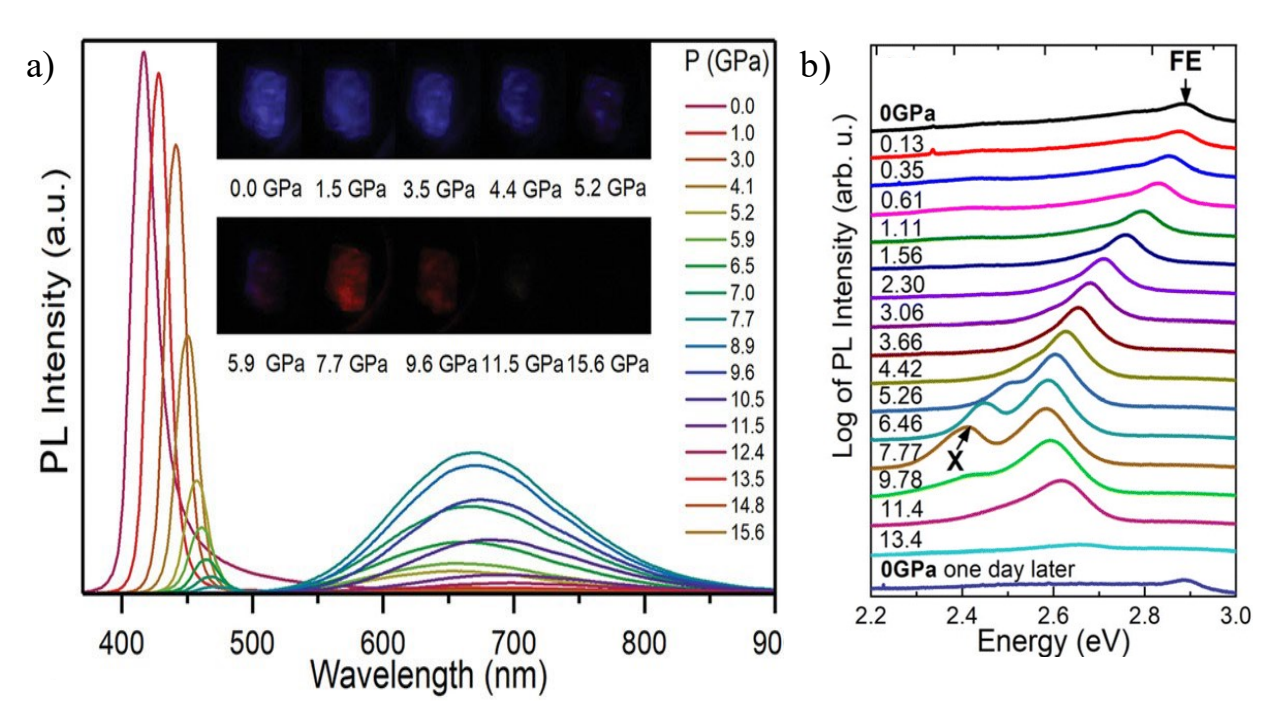


Figure 14. Pressure-induced change in PL nature of RP-type 2D HOIPs. (a) In situ PL spectra upon compression to 15.6 GPa of (PEA)₂PbBr₄ [52] and (b) In situ PL spectra upon compression to 13.4 GPa of Tz₂PbBr₄ [56].

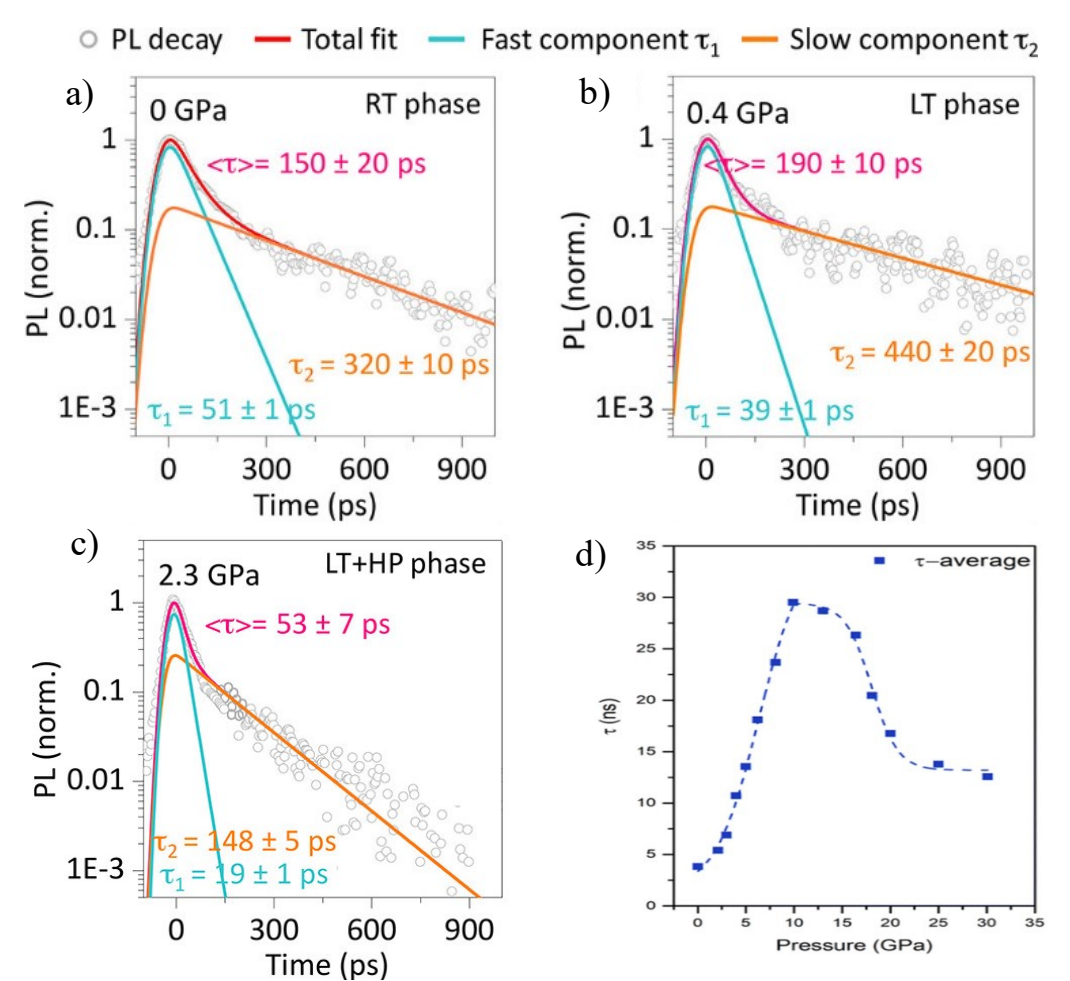


Figure 15. Pressure-induced charge carrier lifetimes of 2D HOIPs. (a), (b), and (c) TRPL spectra of (BA)₂PbI₄ at 0, 0.4, and 2.3 GPa, respectively [21]. (d) Average PL lifetime as a function of pressure of (2meptH₂)PbCl₄ [34].

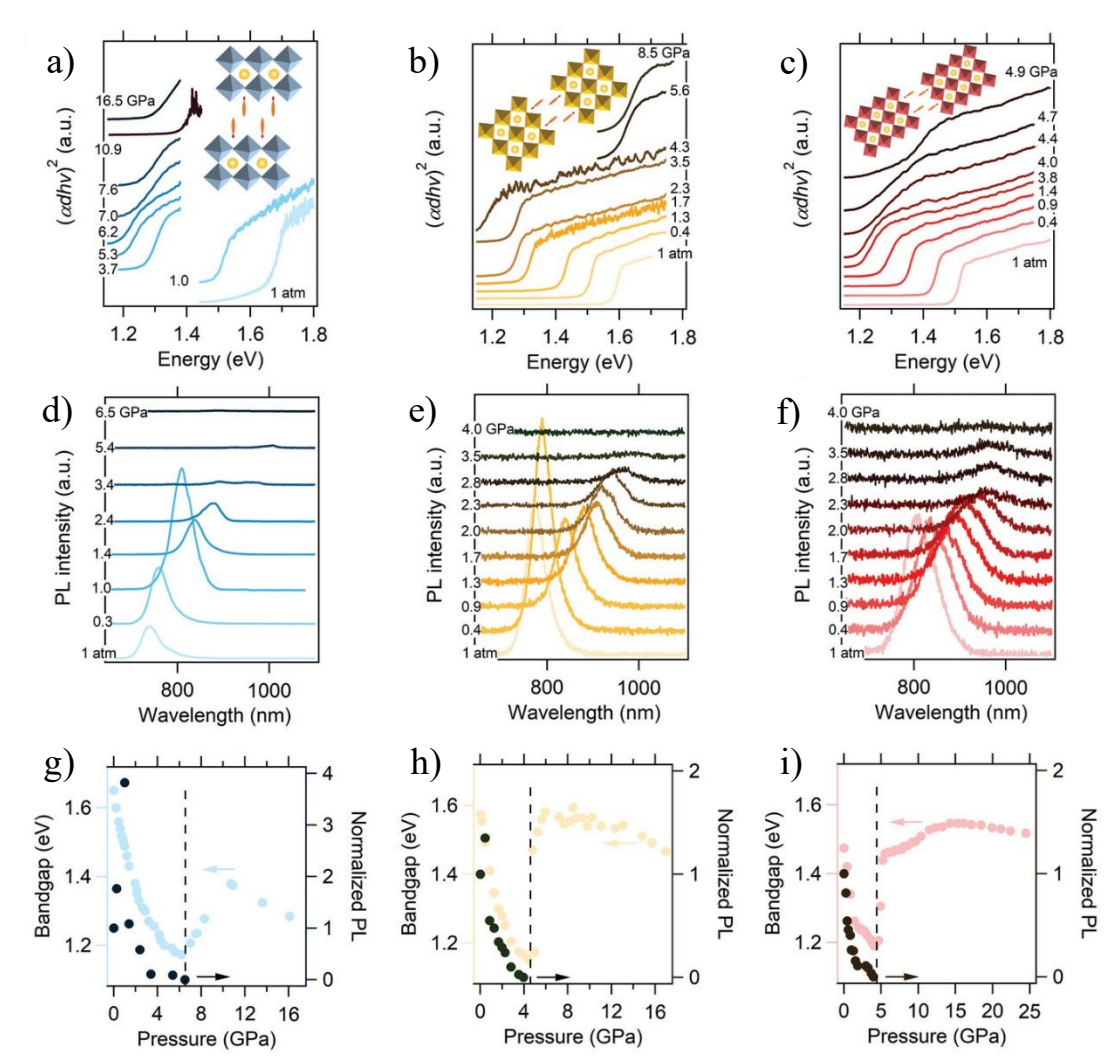


Figure 16. Tuning of optoelectronic properties of $(BA)_2(MA)_{n-1}Sn_nI_{3n+1}$ RP family. Absorption spectra upon compression for (a) $(BA)_2(MA)Sn_2I_7$, (b) $(BA)_2(MA)_2Sn_3I_{10}$, and (c) $(BA)_2(MA)_3Sn_4I_{13}$. PL spectra upon compression for (d) $(BA)_2(MA)Sn_2I_7$, (e) $(BA)_2(MA)_2Sn_3I_{10}$, and (f) $(BA)_2(MA)_3Sn_4I_{13}$. Bandgap as a function of pressure for (g) $(BA)_2(MA)Sn_2I_7$, (h) $(BA)_2(MA)_2Sn_3I_{10}$, and (i) $(BA)_2(MA)_3Sn_4I_{13}$ [75].

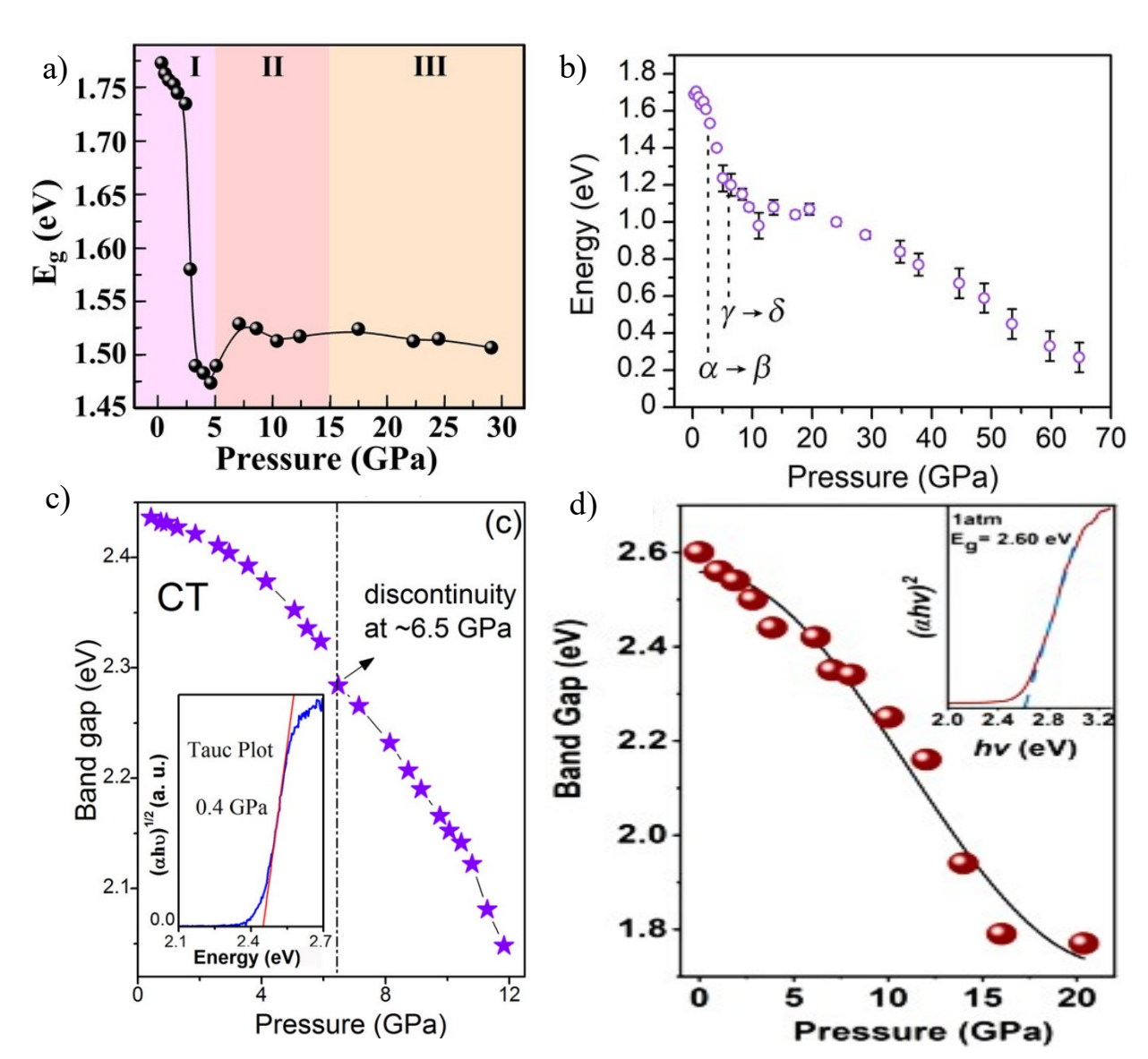


Figure 17. Pressure-induced bandgap behavior of Cu-based 2D HOIPs. Bandgap as a function of pressure for (a) (PMA)₂CuBr₄ and (b) (EA)₂CuBr₄ [79,80]. Bandgap as a function of pressure for (c) DABCuCl₄ and (d) (PEA)₂CuCl₄ [81,82].

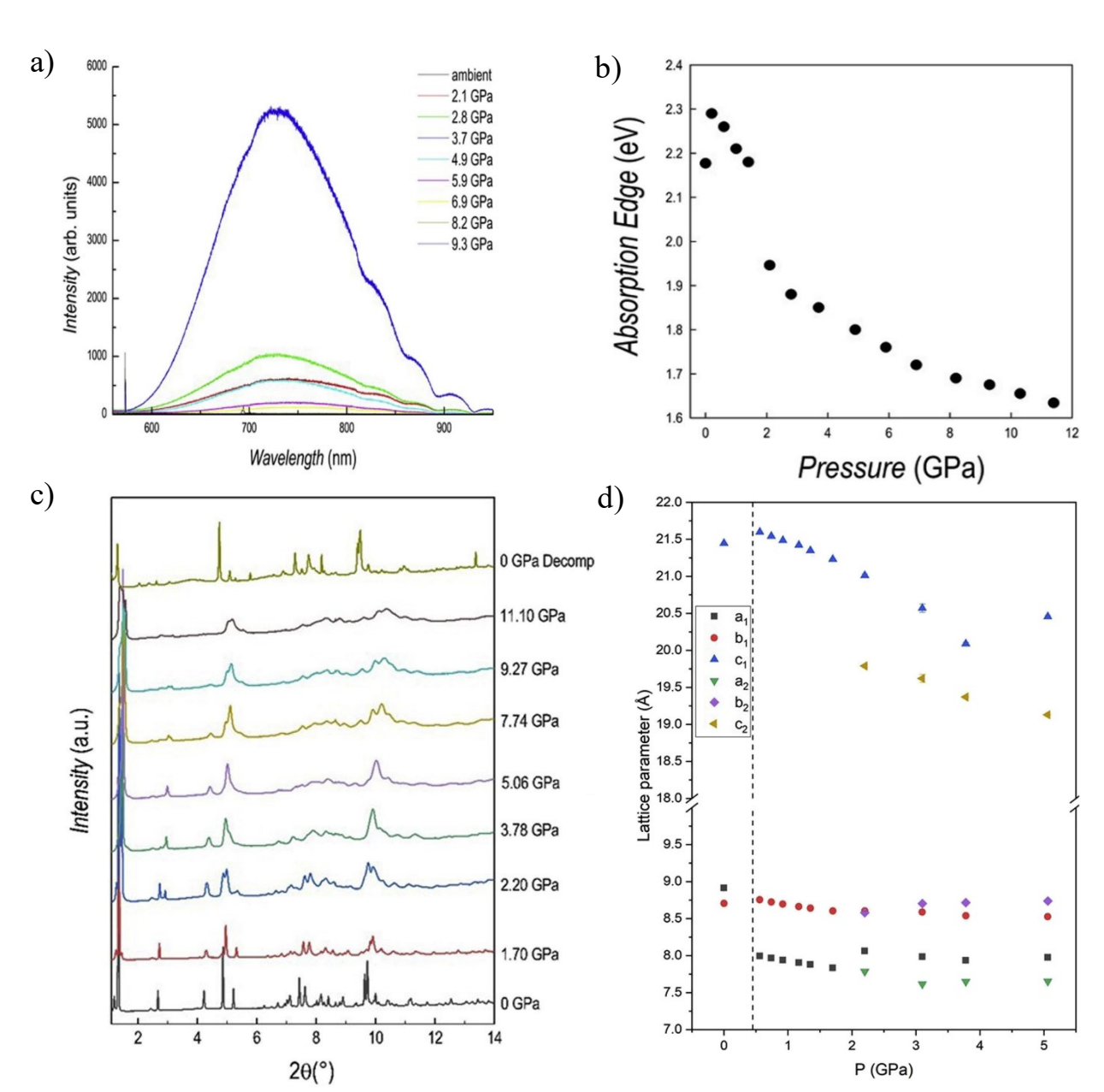


Figure 18. Behavior of (DA)₂GeI₄ under high pressure. (a) PL spectra upon compression, and (b) absorption edge as a function of pressure, (c) XRD spectra upon compression, and (d) unit cell parameters as functions of pressure [84].

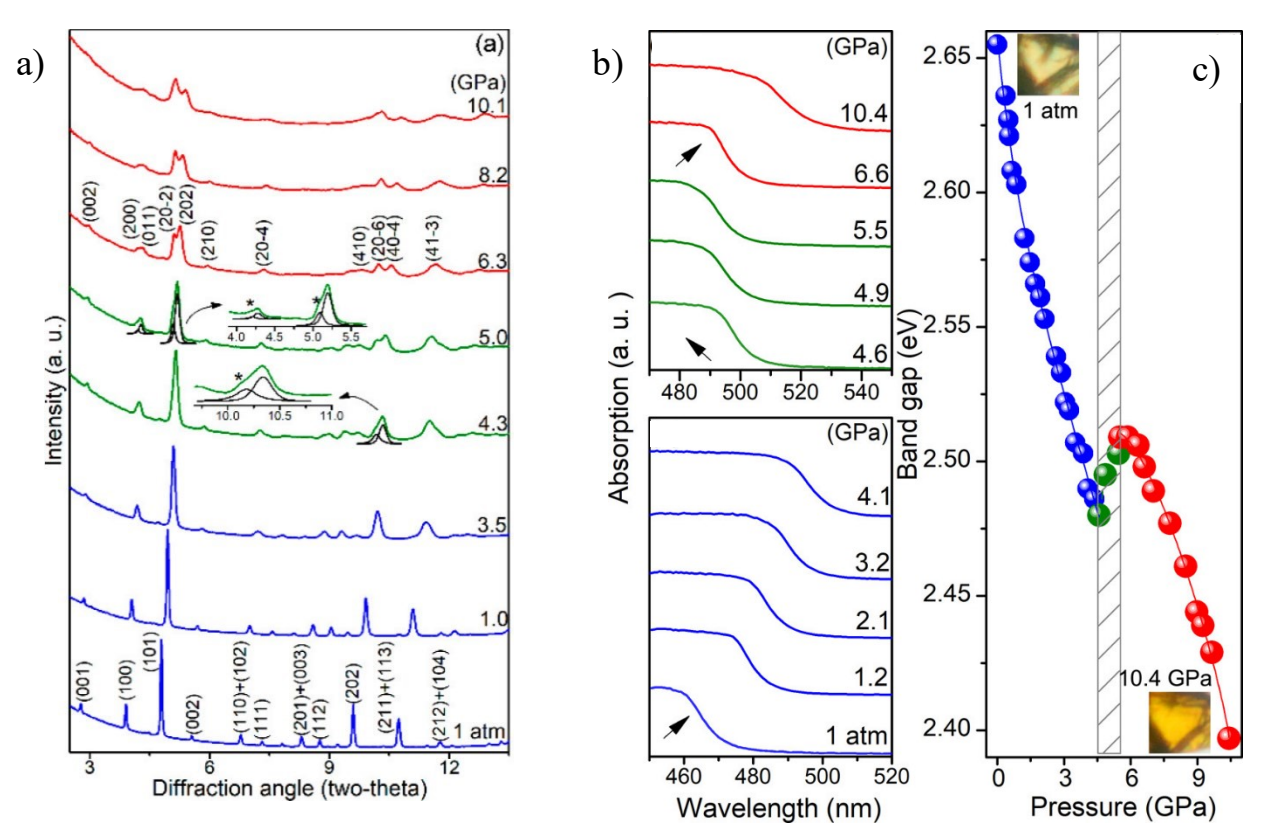


Figure 19. Behavior of MA₃Bi₂Br₉ under high pressure. (a) ADXRD spectra upon compression, (b) UV-Vis absorption spectra upon compression, and (c) bandgap as a function of pressure [85].

Data availability statements

† No new data were generated in support of this review.